Argonne NATIONAL LABORATORY

ANL/LWRS-15/01

System-Level Heat Transfer Analysis, Thermal-Mechanical Cyclic Stress Analysis, and Environmental Fatigue Modeling of a Two-Loop Pressurized Water Reactor: A Preliminary Study

Nuclear Engineering Division

About Argonne National Laboratory

Argonne is a U.S. Department of Energy laboratory managed by UChicago Argonne, LLC under contract DE-AC02-06CH11357. The Laboratory's main facility is outside Chicago, at 9700 South Cass Avenue, Argonne, Illinois 60439. For information about Argonne and its pioneering science and technology programs, see www.anl.gov.

DOCUMENT AVAILABILITY

Online Access: U.S. Department of Energy (DOE) reports produced after 1991 and a growing number of pre-1991 documents are available free via DOE's SciTech Connect (http://www.osti.gov/scitech/)

Reports not in digital format may be purchased by the public from the National Technical Information Service (NTIS):

U.S. Department of Commerce
National Technical Information Service
5301 Shawnee Rd
Alexandria, VA 22312
www.ntis.gov
Phone: (800) 553-NTIS (6847) or (703) 605-6000
Fax: (703) 605-6900
Email: **orders@ntis.gov**

Reports not in digital format are available to DOE and DOE contractors from the Office of Scientific and Technical Information (OSTI):

U.S. Department of Energy
Office of Scientific and Technical Information
P.O. Box 62
Oak Ridge, TN 37831-0062
www.osti.gov
Phone: (865) 576-8401
Fax: (865) 576-5728
Email: **reports@osti.gov**

Disclaimer

This report was prepared as an account of work sponsored by an agency of the United States Government. Neither the United States Government nor any agency thereof, nor UChicago Argonne, LLC, nor any of their employees or officers, makes any warranty, express or implied, or assumes any legal liability or responsibility for the accuracy, completeness, or usefulness of any information, apparatus, product, or process disclosed, or represents that its use would not infringe privately owned rights. Reference herein to any specific commercial product, process, or service by trade name, trademark, manufacturer, or otherwise, does not necessarily constitute or imply its endorsement, recommendation, or favoring by the United States Government or any agency thereof. The views and opinions of document authors expressed herein do not necessarily state or reflect those of the United States Government or any agency thereof, Argonne National Laboratory, or UChicago Argonne, LLC.

ANL/LWRS-15/01

System-Level Heat Transfer Analysis, Thermal-Mechanical Cyclic Stress Analysis, and Environmental Fatigue Modeling of a Two-Loop Pressurized Water Reactor: A Preliminary Study

Subhasish Mohanty, William Soppet, Saurin Majumdar, and Ken Natesan

Nuclear Engineering Division, Argonne National Laboratory

April 2015

This page intentionally left blank

ABSTRACT

This report provides an update on an assessment of environmentally assisted fatigue for light water reactor components under extended service conditions. This report is a deliverable in April 2015 under the work package for environmentally assisted fatigue under DOE's Light Water Reactor Sustainability program. In this report, updates are discussed related to a system-level preliminary finite element model of a two-loop pressurized water reactor (PWR). Based on this model, system-level heat transfer analysis and subsequent thermal-mechanical stress analysis were performed for typical design-basis thermal-mechanical fatigue cycles. The in-air fatigue lives of components, such as the hot and cold legs, were estimated on the basis of stress analysis results, ASME in-air fatigue life estimation criteria, and fatigue design curves. Furthermore, environmental correction factors and associated PWR environment fatigue lives for the hot and cold legs were estimated by using estimated stress and strain histories and the approach described in NUREG-6909. The discussed models and results are very preliminary. Further advancement of the discussed model is required for more accurate life prediction of reactor components. This report only presents the work related to finite element modelling activities. However, in between multiple tensile and fatigue tests were conducted. The related experimental results will be presented in the year-end report.

This page intentionally left blank

TABLE OF CONTENTS

LIST OF FIGURES

LIST OF TABLES

ABBREVIATIONS

ANL	Argonne National Laboratory
CL	Cold Leg
DOE	Department of Energy
FE	Finite Element
FEA	Finite Element Analysis
HL	Hot Leg
ID	Inside Diameter
LOCA	Loss of Coolant Accident
LWR	Light Water Reactor
LWRS	Light Water Reactor Sustainability
OD	Outside Diameter
PTS	Pressurized Thermal Shock
PWR	Pressurized Water Reactor
SCC	Stress Corrosion Cracking
SG	Steam Generator
SS	Stainless Steel
TMF	Thermal Mechanical Fatigue

ACKNOWLEDGMENTS

This research was supported through the U.S. Department of Energy's Light Water Reactor Sustainability program under the work package of environmental fatigue study, program manager Dr Jeremy Busby.

This page intentionally left blank

1 Introduction

System-level computer modeling of complex nuclear systems is increasingly becoming a trend due to the availability of advanced multi-physics computer programs and the increasing use of multiprocessor-based parallel computing hardware and software. Recently, many works have been published on thermal-hydraulics simulations of fluid flow and heat transfer in a single reactor component or in a complex large-scale assembly [1-7]. This type of system-level thermal-hydraulics model helps to better understand and to accurately predict the fluid flow and heat transfer not only in individual components but also the overall system and the interaction with each other. Along a similar line, computational structural mechanics analysis is increasingly being used to perform stress and fracture mechanics analysis under complex component/assembly-level multi-axial stress states. For example, recent advances in 3-D finite element analyses (FEA) code and associated improvements in multi-physics modeling capability (e.g., thermal-mechanical stress analysis) and fracture mechanics simulation capability allow more accurate 3-D stress and structural integrity analysis of reactor components not only under combined thermal-mechanical loading but also under multi-axial component/assembly-level stress states [8-10]. In addition to the above-mentioned multi-physics thermal-mechanical stress analysis, the present-generation FEA code also allows determination of the effect of other field variables, such as the effect of neutron dose on the 3D stress state of reactor structural components [11,12]. Furthermore, advances in FEA tools for 3-D fracture mechanics and crack propagation allow accurate prediction of the structural integrity of reactor components under severe accident conditions, such as loss-of-coolant accidents (LOCAs). For example, propagation of preexisting stress corrosion cracking (SCC) in steam generator tubes and the associated rupture pressure can be predicted accurately under LOCA [13]. Similarly, in reactor pressure vessels and other primary pressure boundary components, the effect of pressurized thermal shock (PTS) under severe accident conditions can be predicted by using 3-D FEA tools [14-19]. Both LOCA and PTS conditions are key elements in the integrity evaluation of nuclear reactor components and require a multidisciplinary effort to link the thermal-hydraulic analysis results to structural and fracture mechanics models. In addition to the multi-physics capability, the current-generation FEA code also allows one to model complex time-dependent material effects. For example, time-dependent creep damage of the reactor pressure vessel under severe accident conditions, such as a LOCA, can be more accurately predicted by using component-scale, 3-D FEA models [20].

The above-mentioned structural analysis examples based on FEA are mostly restricted to a single component under static or quasi-static transient loading. However, a few studies have been done involving thermal-mechanical fatigue modeling using system-level 3-D models. Also, at present, most of the work related to fatigue evaluation in reactor environments is based on stress analysis at the individual component level combined with estimation of the associated fatigue life using stress/strain life curves [21-24]. However, as part of the Light Water Reactor Sustainability (LWRS) program sponsored by the Department of Energy (DOE), Argonne National Laboratory (ANL) is trying to develop a more mechanistic-based fatigue evaluation approach [25,26] under realistic multi-physics and multi-axial stress states. Under this program ANL is trying to develop a multi-component finite element (FE) model for multi-physics and system-level stress analysis and associated fatigue life evaluation under thermal-mechanical cyclic loading. For the purpose, in the present work, we developed preliminary FE models for a Westinghouse-type two-loop pressurized water reactor (PWR). Based on

the FE models, system-level thermal-mechanical fatigue (TMF) analyses were performed. Furthermore, these TMF results were used for in-air and environmental fatigue life estimation of some key components such as the reactor cold and hot legs. The related model and calculated results are discussed below.

2 Finite Element Modeling

This section summarizes the 3-D FE models discussed in this report. The FE models were developed both for heat transfer analysis and for thermal-mechanical cyclic stress analysis.

2.1 System level 3-D solid model

Finite element models were developed for system-level TMF analysis of a Westinghouse-type two-loop PWR. The models were developed by using commercially available ABAQUS FE software [27]. The FE models were based on approximate geometry determined from publicly available literatures [28-32]. In the assembly-level model, only major reactor parts such as the pressure vessel, steam generator outer shell, and hot and cold leg pipes were considered. Figure 1 shows the resulting assembly-level 3-D solid model of the 2-loop PWR considered in this work. Figure 2 shows a quarter section of the overall assembly, outlining the inside diameter (ID) surface of different components.

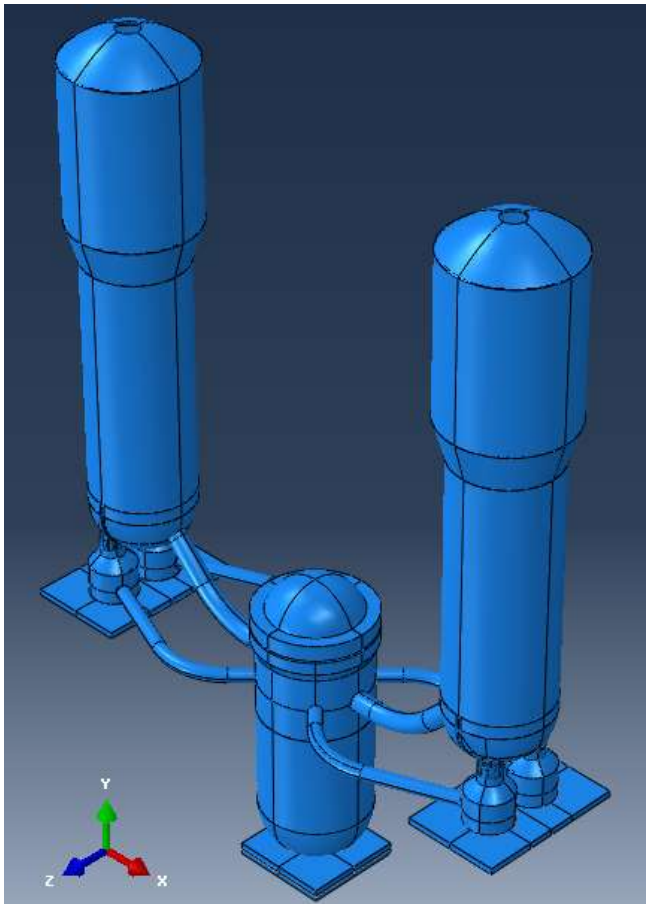

Figure 2.1 Assembly-level 3-D solid model of a two-loop PWR

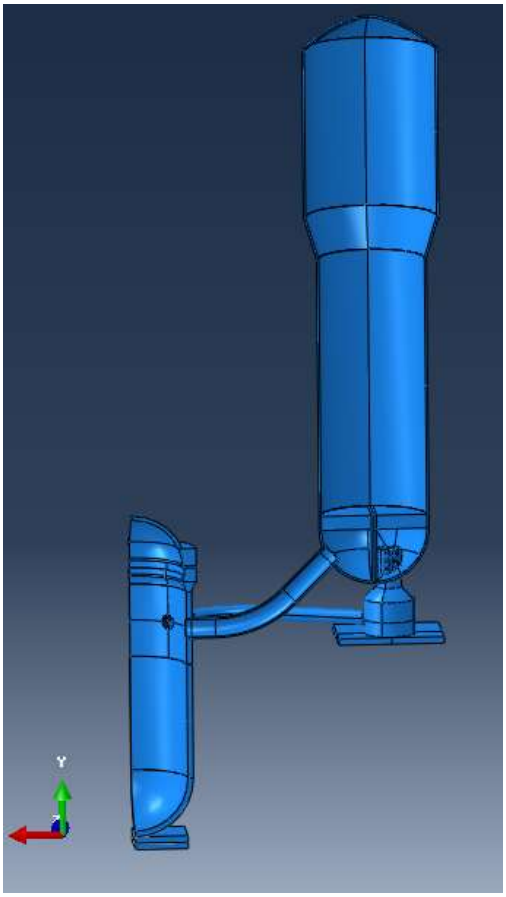

Figure 2.2 Quarter assembly showing ID surface of different components

For simplicity, the surge line and pressurizer were not considered in the assembly-level model. Also, a simplified coolant pump model was assumed, and only the top section that connects both the steam generator and cold leg was considered. However, in the future, for more detailed analysis, the surge line, pressurizer and other important components will be considered. The assembly-level model was developed by using 3-D solid models of individual components with single or multiple sections. The 3-D models were developed by using ABAQUS CAE software. The individual sections or components were appropriately constrained to maintain their locations with respect to the global assembly. In the assembly model, the individual sections were tied together by using tie constraints. The bottom section of the reactor pressure vessel (RPV) was tied to a base plate, which was attached to the ground and constrained in all directions. Similarly, the coolant pumps were tied to additional base plates. However, in contrast to the RPV base plates, the coolant pump base plates were only restricted in the vertical direction and were allowed to move along both horizontal directions. This condition was designed to mimic the real reactor conditions, allowing free thermal expansion. However, note that the above boundary conditions are simplified assumptions and do not necessarily represent the exact boundary conditions in a real reactor. In addition, in the present assembly-level model, we did not consider the plane of symmetries. In the future we intend to add unsymmetrical components such as a surge line and pressurizer, and it may not be possible to implement a symmetric boundary condition in the system-level reactor model. Hence, in the present model, symmetric boundary conditions were not considered for

possible future amendment. The same assembly-level 3-D model was used for both heat transfer analysis and subsequent sequential structural analysis.

2.2 Finite element mesh

The individual components in the reactor assembly were FE meshed by using 3-D brick elements. We chose DC3D8, 8-node linear heat transfer elements to mesh the individual components in the assembly-level heat transfer models. The corresponding C3D8, 8-node linear elements were used for the stress analysis models. The assembly has a total of 82762 DC3D8 elements for heat transfer models or C3D8 elements for structural analysis models. Table 2.1 shows the number of elements used for individual components and the respective material type used in the simulation. Figure 2.3 shows the full assembly-level FE mesh of the outside diameter (OD) surface, whereas Figure 2.4 shows the quarter section mesh for the ID surface.

Table 2.1 Number of heat transfer or structural analysis finite elements in PWR assembly models

Component name	Total number of components	Material type	Total number of DC3D8/C3D8 elements
Pressure vessel	1	SA-508 (LAS)	10806
Steam generator shell	2	SA-508 (LAS)	2x17628 = 35256
Hot leg pipe	2	SA-376 (SS)	2x2014 = 4028
Cold leg pipe	4	SA-376 (SS)	4x3204=12816
Coolant pump	4	SA-376 (SS)	4x4164=16656
RPV base plate	1	Fictitious large stiffness material	800
Coolant pump base plate	4	Fictitious large stiffness material	4x600=2400
Total number of elements in assembly			82762

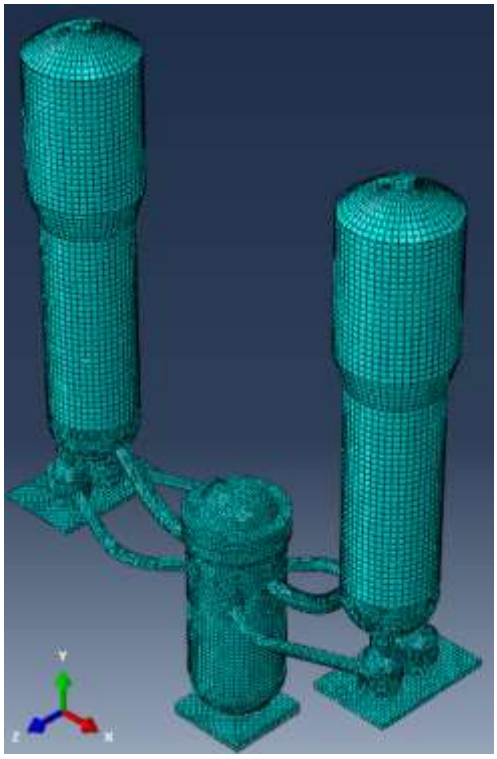

Figure 2.3 Full system-level FE mesh of two-loop PWR

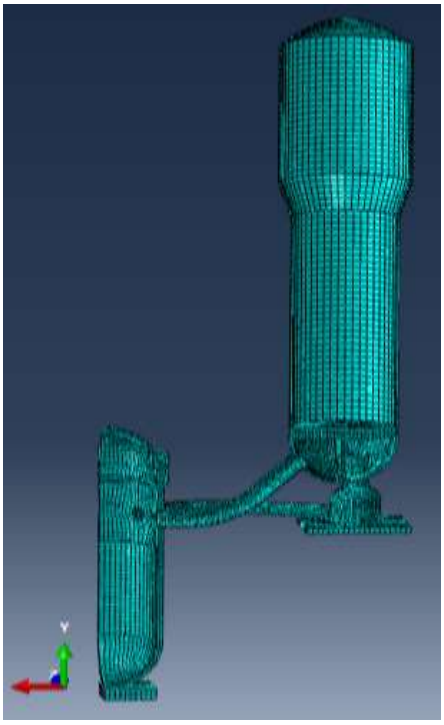

Figure 2.4 Quarter section FE mesh of two-loop PWR showing ID surface

2.3 Heat transfer model

An uncoupled heat transfer analysis was performed by multiple steps of transient heat transfer analysis. The heat transfer analysis was performed with ABAQUS software, for which the variational form of the governing energy balance equation can be given as [27]:

$$\int_V \rho \dot{U}\, \delta\theta dV + \int_V \frac{\partial \delta\theta}{\partial x}.k.\frac{\delta\theta}{\partial x} dV = \int_S \delta\theta q dS \tag{2.1}$$

where ρ is density of material, V is the volume of solid material with surface area S, and q is the heat flux per unit area flowing into or out of the body. Also in Eq. 2.1, U is the material internal energy, which can be expressed in terms of the temperature-dependent specific heat $c(\theta)$ as:

$$c(\theta) = \frac{dU}{d\theta} \tag{2.2}$$

The heat conduction is assumed to be governed by the Fourier law and can be expressed in terms of the temperature-dependent thermal conductivity (θ) :

$$f = -k(\theta)\frac{\partial \theta}{\partial x} \tag{2.3}$$

The surface heat flux q in Eq. 2.1 can be expressed in terms of the temperature-dependent film coefficient $h(\theta)$ as:

$$q = h(\theta)(\theta - \theta_0) \tag{2.4}$$

In ABAQUS, we defined all the ID surface boundaries with time-dependent temperature sinks and the convective film condition. Two repetitive cycles were simulated each with four transient heat transfer steps. At the initial condition, all the material volumes were subjected to a temperature of 37.78 ^{o}C. Before the start of cyclic heat transfer analysis, additional transient heat transfer analysis was performed to bring up/down the boundary condition temperature to the starting temperature of the first cycles. Nine heat transfer steps were performed over the entire simulation duration. During the first step, all the OD surfaces were defined with the ambient temperature boundary condition of 37.78 ^{o}C and convective film condition. The convective film coefficient h for the ambient convective film condition was assumed to be 100 W/m^2-K [33]. The temperature-dependent film coefficient was defined for all other temperature boundary conditions. The highest temperature considered for the boundary condition was 315.56 ^{o}C. The highest film coefficient corresponding to this temperature was assumed equal to 7155 W/m^2-K. Different ID surfaces were defined with different cyclic temperature boundary conditions. For the purpose, we used the design-basis temperature and pressure transients given in NUREG/CR-6909 [21]. The transients were used to make two temperature or pressure cycles. In between two temperature/pressure cycles, sufficient time was maintained to reduce the ID/OD temperature (simulated through heat transfer analysis) to its original temperature. Figure 2.5 shows the temperature and pressure cycles applied to the ID surface of the reactor pressure vessel and hot leg. The temperature and pressure cycles shown in Figure 2.5 were scaled appropriately to develop the boundary temperature and pressure cycles for the ID surface of the cold leg, as well as the shell feed water section and shell steam section of

the steam generator. The resulting boundary temperature and pressure cycles are shown in Figures 2.6, 2.7, and 2.8 for the cold leg, feed water section, and steam section, respectively. Note that the temperature and pressure cycles were chosen to simulate typical reactor heat-up/cool-down cycles and do not necessarily represent actual reactor conditions. Table 2.2 gives the transient heat transfer step number and associated step time with respect to the applied boundary temperature for the RPV ID surface, and these data are for future reference in the later part of this report.

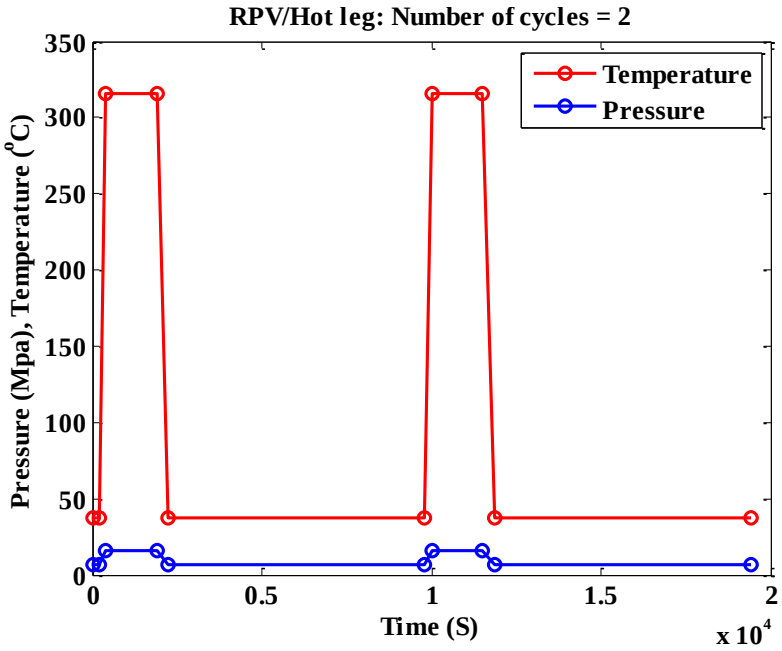

Figure 2.5 Temperature and pressure boundary conditions applied to the ID surfaces of RPV and hot leg

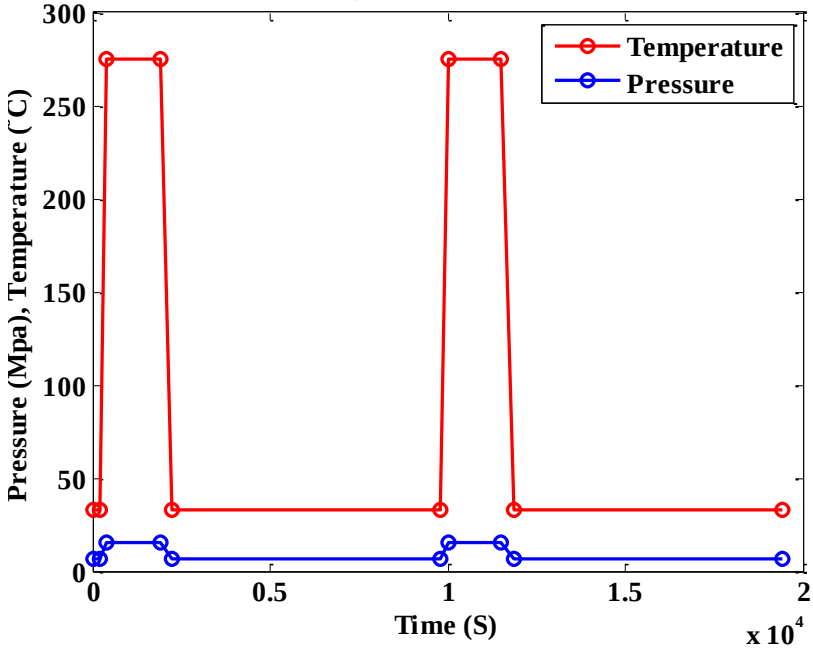

Figure 2.6 Temperature and pressure boundary conditions applied to the ID surfaces of cold leg

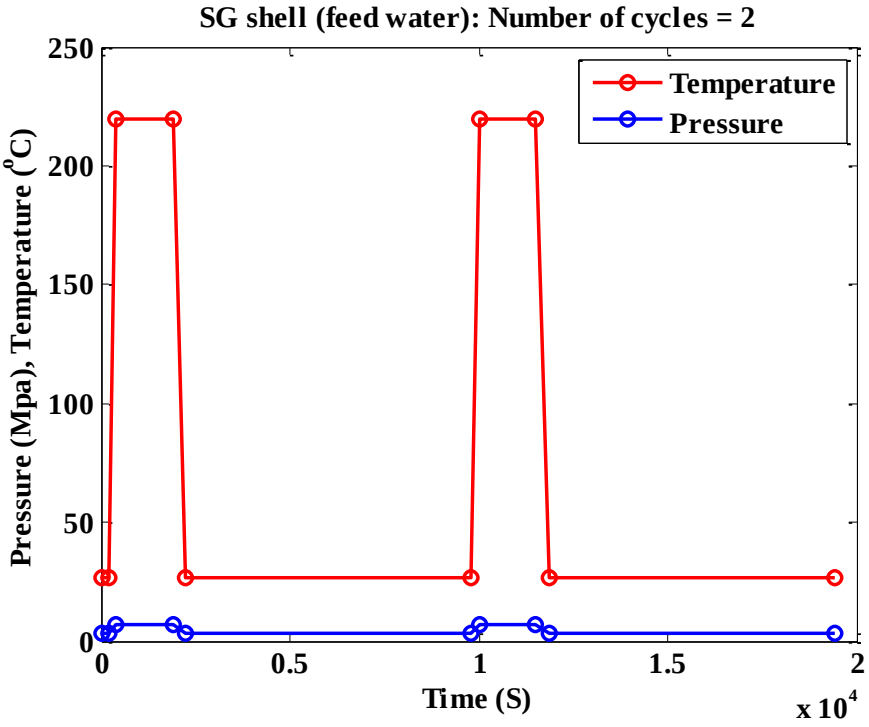

Figure 2.7 Temperature and pressure boundary conditions applied to the ID surfaces of SG feed water section

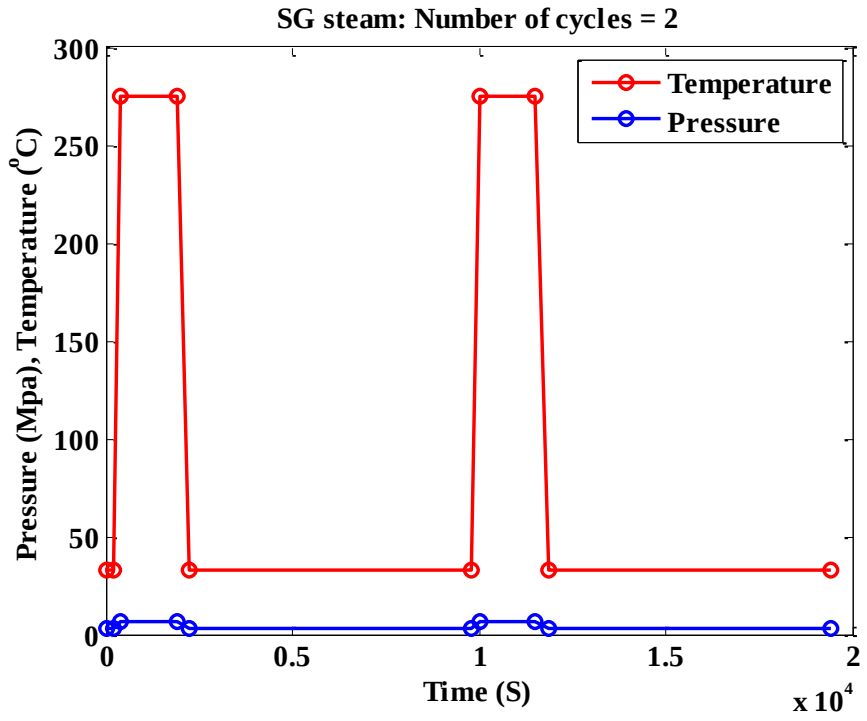

Figure 2.8 Temperature and pressure boundary conditions applied to the ID surfaces of SG steam section

Table 2.2 Transient heat transfer step number and associated RPV ID temperature boundary conditions

Cycle no.	0	1				2			
Step no.	1	2	3	4	5	6	7	8	9
End step time (s)	200	400	1,900	2,250	9,810	10,010	11,510	11,860	19,420
Start temp. (^{o}C)	37.78	37.78	315.56	315.56	37.78	37.78	315.56	315.56	37.78
End temp. (^{o}C)	37.78	315.56	315.56	37.78	37.78	315.56	315.56	37.78	37.78

2.4 Structural analysis cases

The structural analyses were performed for the following cases:

a) Only cyclic pressure

b) Only cyclic temperature

c) Both cyclic pressure and temperature

The structural analysis cases under pure temperature or pure pressure loading were used to assess the contribution of individual temperature and pressure loading on overall stress analysis results performed under combined temperature and pressure loading. For the three cases, nine stress analyses steps were performed to model the ID boundary temperature and pressure cycles shown in Figures 2.5 to 2.8. For stress analysis involving temperature, the heat transfer analysis was performed first, then the resulting temperatures at individual nodes were transferred to the respective structural analysis steps to perform the pure thermal stress analysis (case a) or the sequentially coupled thermal-mechanical stress analysis (case c).

2.5 Material properties for heat transfer and structural analysis model

The heat transfer and stress analysis FE models were developed by using temperature-dependent thermal and mechanical material properties data given in Ref. [23], which were originally considered from the ASME Boiler and Pressure Vessel Code [35]. In this preliminary model, because elastic structural analysis is considered, it is sufficient to consider only the elastic modulus and Poisson ratio. The present FE model uses length in mm, stress in MPa, and temperature in ^{o}C. The original data taken from Ref. [23] employed British units, which were scaled appropriately to use in the present FE models. The material properties data given in [23] are for SA-508 carbon steel (or 508 low alloy steel) and SA-376 stainless steel (equivalent of 316 stainless steel). Figures 2.9 to 2.13 show the temperature-dependent

elastic modulus, mean coefficient of thermal expansion, thermal conductivity, diffusivity, and specific heat capacity in SI units, respectively. The densities were assumed to be temperature independent and were considered to be 8027 and 7750 kg/m^3 for SA-376 and SA-508, respectively. Similarly, the Poisson ratios were assumed temperature independent and were considered to be 0.31 and 0.3 for SA-376 and SA-508, respectively.

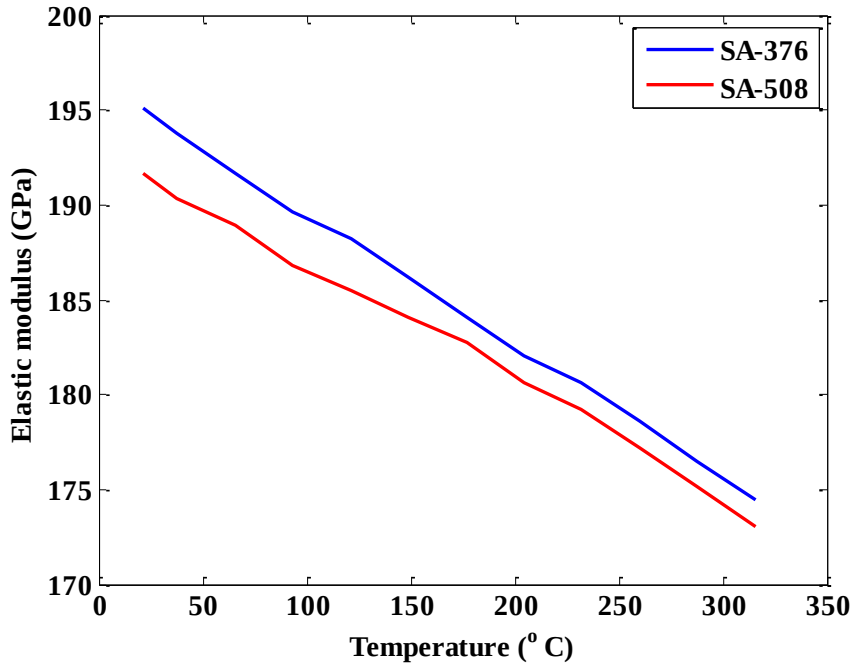

Figure 2.9 Temperature-dependent elastic modulus for SA-376 and SA-508

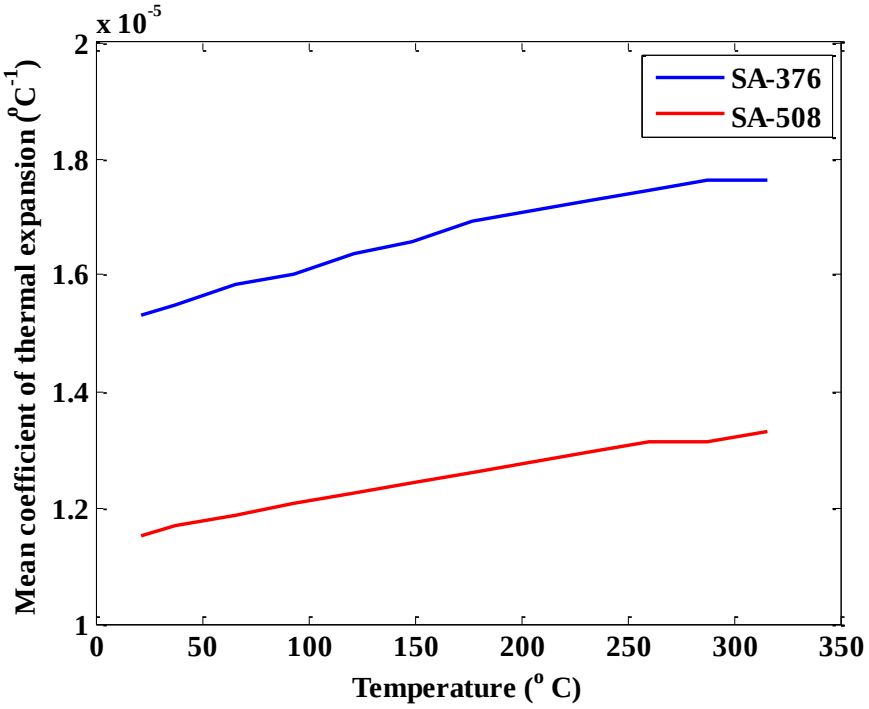

Figure 2.10 Temperature-dependent mean coefficient of thermal expansion for SA-376 and SA-508

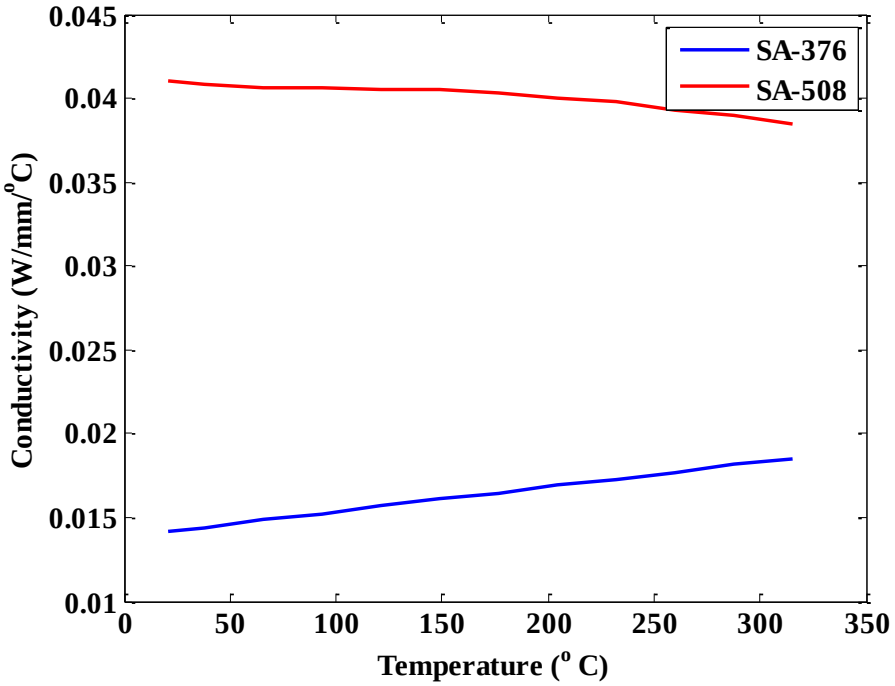

Figure 2.11 Temperature-dependent thermal conductivity for SA-376 and SA-508

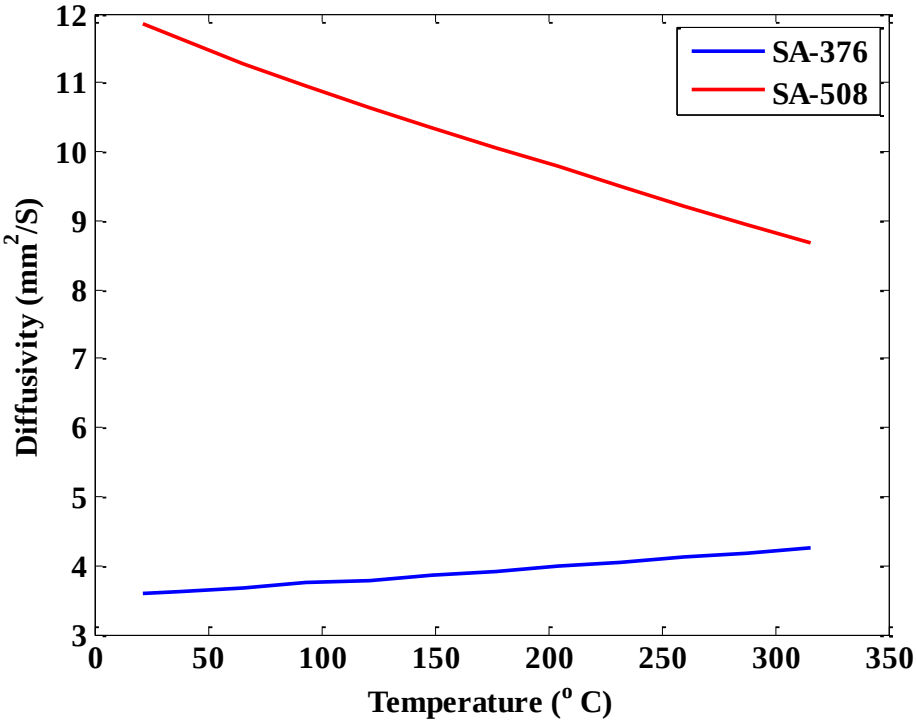

Figure 2.12 Temperature-dependent diffusivity for SA-376 and SA-508

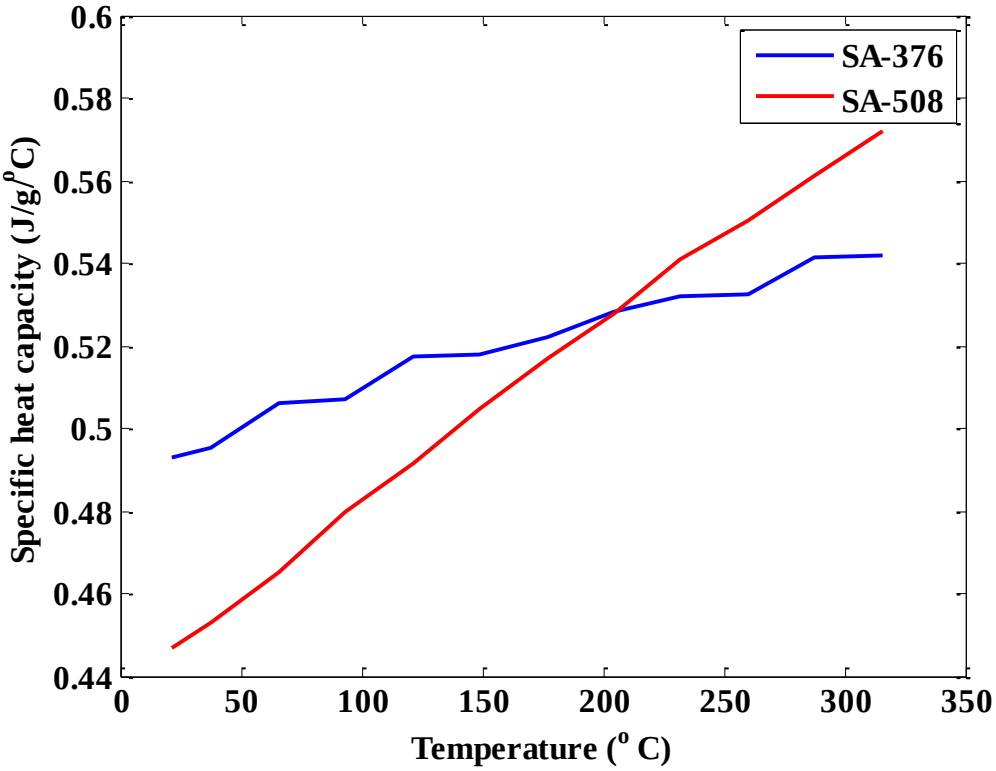

Figure 2.13 Temperature-dependent specific heat capacity for SA-376 and SA-508

3 Results of Heat Transfer Analysis

As discussed above, we have developed an assembly-level heat transfer model to estimate the temperature profile at a given location and at a given time. Some of the important results from this model are discussed below.

3.1 Selection of artificial convective heat transfer coefficient

Selection of appropriate heat transfer coefficient (Eq. 2.4) is important for convective heat transfer analysis. Accurate heat transfer coefficients have to be estimated either based on rigorous thermo-hydraulic experiments or through computational fluid dynamics models. However, such analysis was beyond our scope. Rather, a simple relation between heat transfer coefficient h and Nusselt number $N_u$was used to estimate a first approximation of the heat transfer coefficient. This relation is given as

$$N_u = \frac{hD_e}{k_w} \tag{3.1}$$

The Nusselt number N_u is estimated from the Dittus-Boelter correlation for turbulent heat transfer:

$$N_u = 0.023Re^{0.8}Pr^n \tag{3.2}$$

In Eqs. 3.1 and 3.2, D_e is the hydraulic diameter (assumed equal to the diameter of the hot leg, i.e. 0.66548 m in the present FE model), k_w is the thermal conductivity of water (0.6096 W/m-K at 300 ^{o}C, [34]), Re is the Reynolds's number (500,000 based on Ref. [7]), and Pr is the Prandtl number (0.8601 at 300 ^{o}C and 15 MPa [34]). Also, the coefficient n in Eq. 3.2 is set equal to 0.3 assuming the fluid is being cooled. With these values, the first approximation of the heat transfer coefficient h was calculated to be 715.5 W/m^2-K. With this coefficient, an initial heat transfer analysis was performed for the above temperature boundary conditions. From the simulation results, we found that the temperature at the ID surface was not reaching the desired boundary value at the highest test temperature. This was possibly due to lower heat-up time and subsequent lower steady-state heating time. In an actual reactor, the individual duration for heat-up, cool-down, and steady-state normal operation will be much higher compared to the time durations considered for the example temperature cycles. However, increasing the duration for individual transient heat transfer steps would increase the overall times for heat transfer analysis computation. This increase would increase the subsequent times for structural analysis computation. To avoid large transient heat transfer time steps, the convective heat transfer coefficient was artificially increased. For example, for 315.56 ^{o}C, the above estimated h was increased by 10 times, to 7155 W/m^2-K. For other temperatures, this film coefficient was linearly scaled. Two heat transfer analysis were performed using h = 715.5 W/m^2-K and 7155 W/m^2-K. Figure 3.1 shows the resulting simulated temperatures at typical OD and ID nodes in the mid-section of the RPV. This figure indicates that the estimated highest ID temperature with h = 715.5 W/m^2-K is much lower compared to the desired highest ID temperature of 315.56 ^{o}C (see Figure 2.5). In contrast, the h = 7155 W/m^2-K case

simulates fairly well the desired boundary condition temperature with the stipulated step time. Hence, we used h = 7155 W/m^2-K for the subsequent heat transfer analysis discussed later. Note that in the sequential structural analysis model, the rate effect (e.g., strain rate) is not modeled; hence, it is not required to consider prototypical temperature ramp-up/down duration. The present structural analysis model only requires an accurate spatial distribution of the nonlinear temperature profile at any given time. For the rate-dependent structural analysis, it is essential to consider prototypical time steps pertinent to particular reactor conditions.

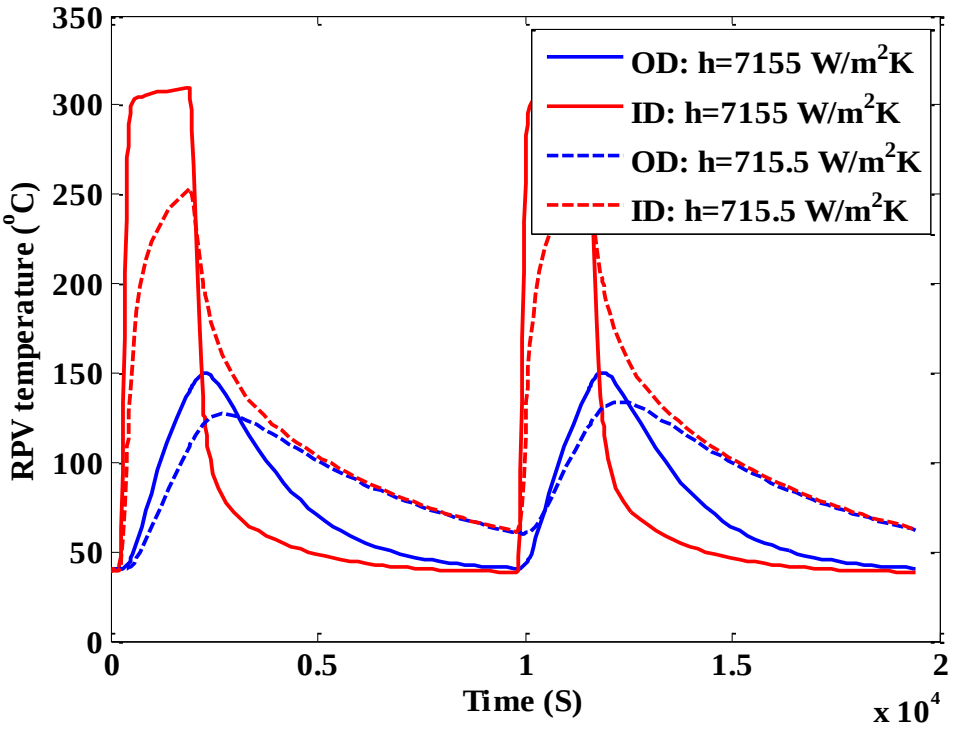

Figure 3.1 Simulated temperature at RPV mid-section OD and ID for different heat transfer coefficients

3.2 Linear versus quadratic heat transfer elements

It is essential to select appropriate heat transfer elements for accurate estimation of the temperature distribution and, at same time, minimize the computational burden. For that purpose, we performed parametric studies considering both linear heat transfer elements (DC3D8) and quadratic heat transfer elements (DC3D20). Both assembly-level FE models were simulated in the batch mode using seven processors of a Linux cluster. From the simulation, we found that the FE model with DC3D8 elements took much less CPU time (approximately 15 minutes) compared to that of the FE model with DC3D20 elements (approximately 45 minutes). In addition, the linear element model generates a smaller output file that can easily be imported to the structural analysis model. At same time, the DC3D8-based heat transfer model gives fairly similar results to those for the DC3D20-based heat transfer model, as shown in Figure 3.2 for the simulated RPV mid-section OD and ID temperature. Hence, we used the DC3D8 elements for subsequent heat transfer models and for the corresponding stress analysis elements (C3D8) in the structural analysis.

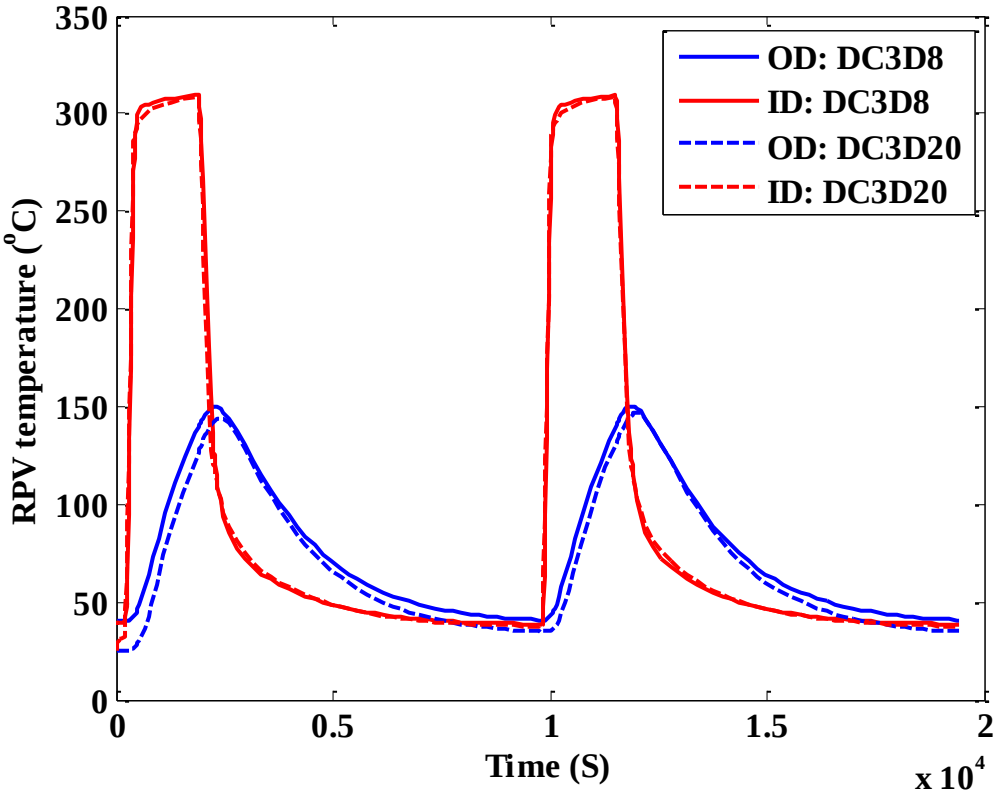

Figure 3.2 Simulated temperature at RPV mid-section OD and ID for DC3D8 and DC3D20 heat transfer elements

3.3 Representative heat transfer analysis results

Based on the cyclic temperature boundary conditions in Figures 2.5 to 2.8, the DC3D8 linear brick elements, and the heat transfer coefficient h = 7155 W/m^2-K, we performed a heat transfer analysis for the full assembly-level model shown in Figure 2.3. Representative results are presented below. Figures 3.3 and 3.4 show the OD and ID surface temperature distribution, respectively, at the end of 1900 seconds, i.e., at the end of step 3 in Table 2.2. Similarly Figures 3.5 and 3.6 show the OD and ID surface temperature distribution, respectively, of the full assembly at the end of 19,420 seconds, i.e., at the end of step 9. Figure 3.7 shows a closer view of the temperature distribution at the end of 1900 seconds in the steam generator (SG) bottom section ID, the hot leg (HL) OD, and the cold leg (CL) OD surfaces. Figures 3.8 and 3.9 show a closer view of the temperature distribution in the HL and CL ID surfaces at the end of 1900 seconds. Similarly, Figures 3.10(a) and (b) show a closer view of the spatial distribution of the temperature in the SG tube sheet at the end of 1900 seconds at its bottom side (toward HL/CL) and at its top side (toward feed water side), respectively.

Time histories of temperatures were estimated at representative locations of different components. For example, Figure 3.11 shows the time histories for simulated temperatures at typical OD and ID nodes in the mid-section of the RPV. Figures 3.12 and 3.13 show the time histories for simulated temperatures at typical OD and ID nodes in the elbow section of the HL and CL, respectively. Figure 3.14 shows the time histories of the simulated temperatures at typical mid-section junction nodes in the tube sheet of the

SG. Figures 3.15 and 3.16 show time histories for simulated temperatures at typical OD and ID nodes in the SG feed water and steam sections, respectively.

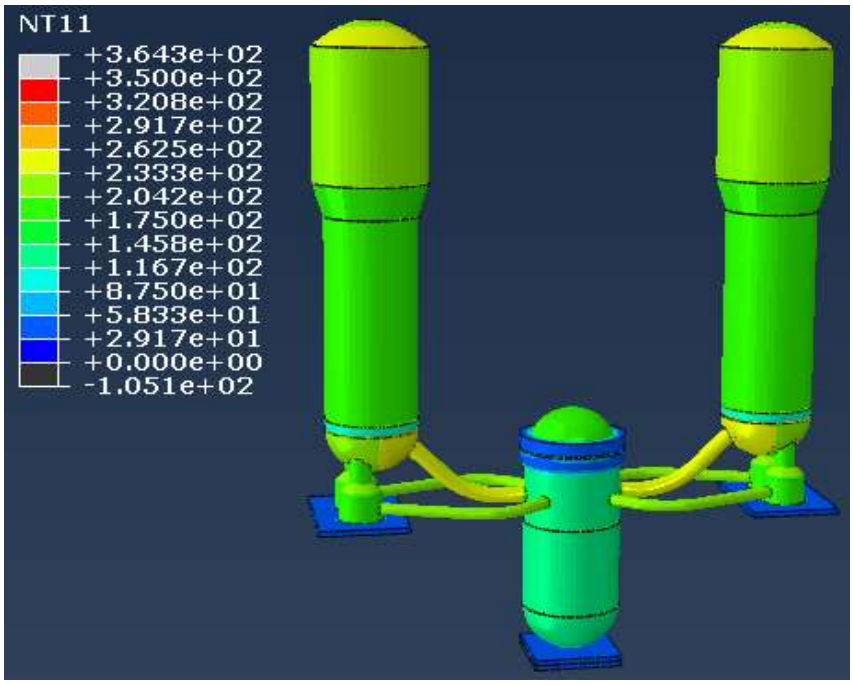

Figure 3.3 Distribution of OD surface temperature of full assembly at the end of 1900 sec

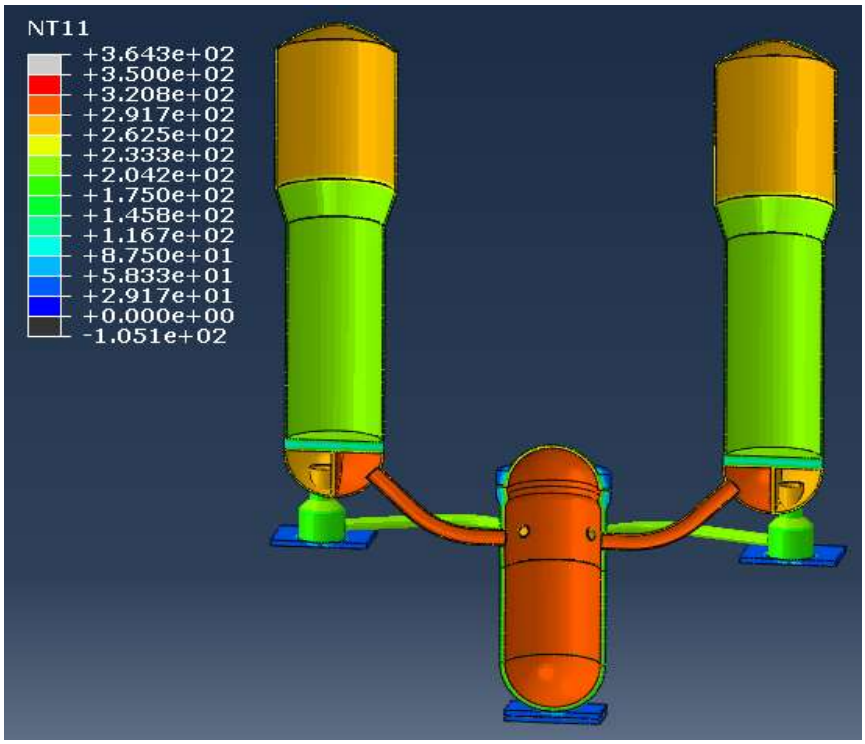

Figure 3.4 Distribution of ID surface temperature of full assembly at the end of 1900 sec

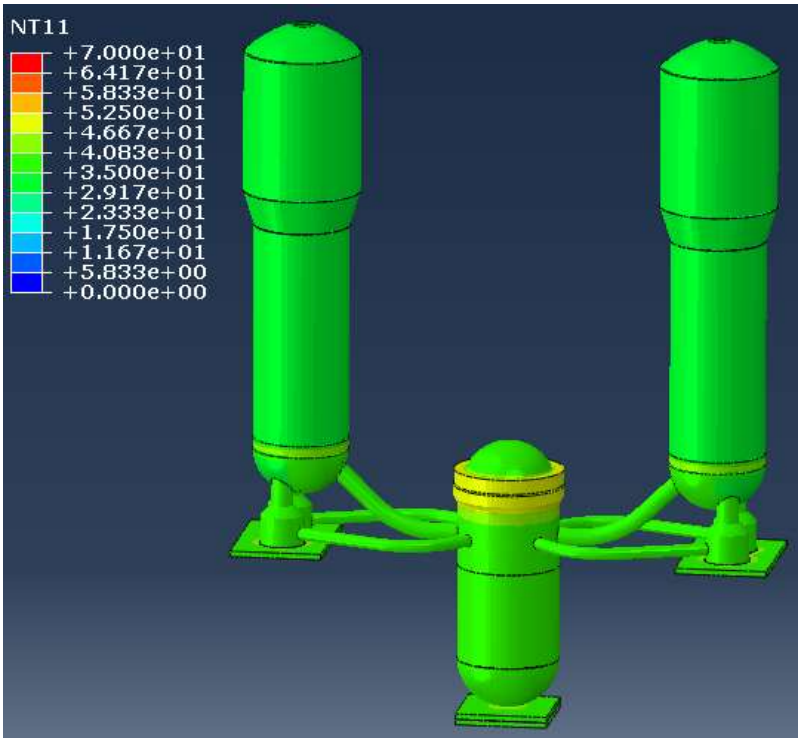

Figure 3.5 Distribution of OD surface temperature of full assembly at the end of 19,420 sec

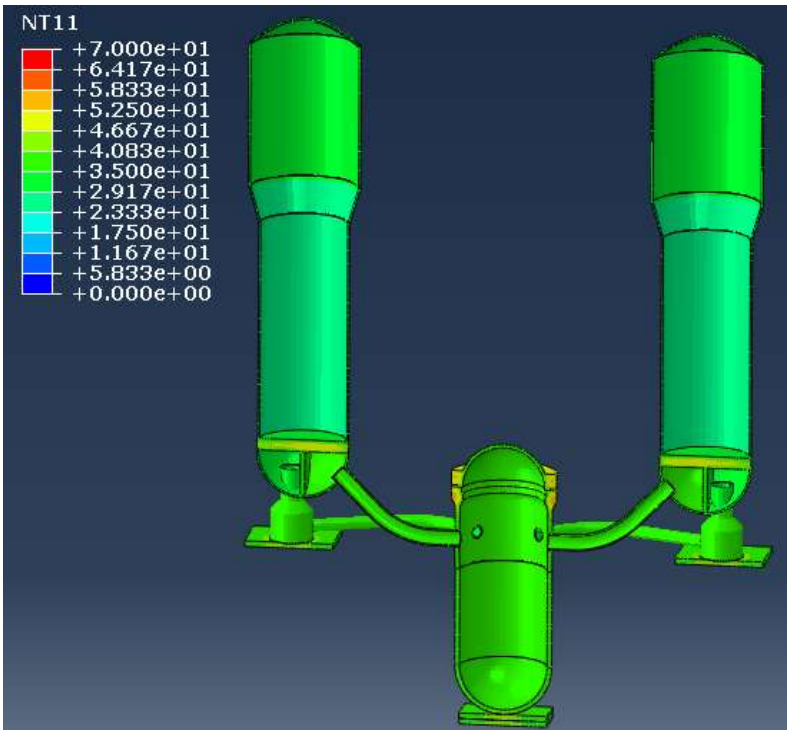

Figure 3.6 Distribution of ID surface temperature of full assembly at the end of 19,420 sec

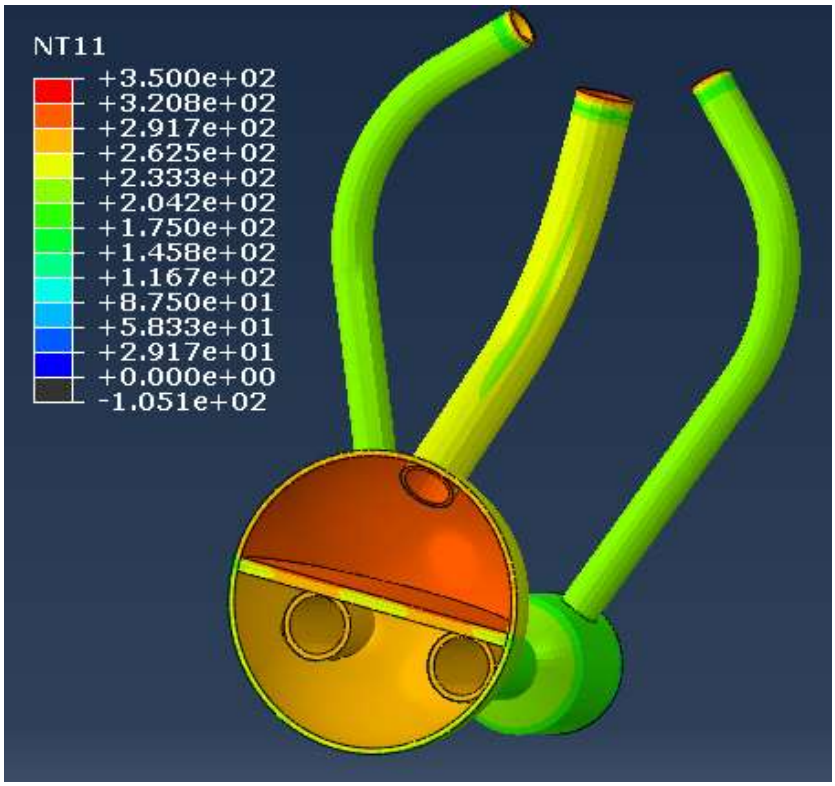

Figure 3.7 Closer view of spatial distribution of temperature in SG bottom section ID, HL OD, and CL OD surfaces at the end of 1900 sec

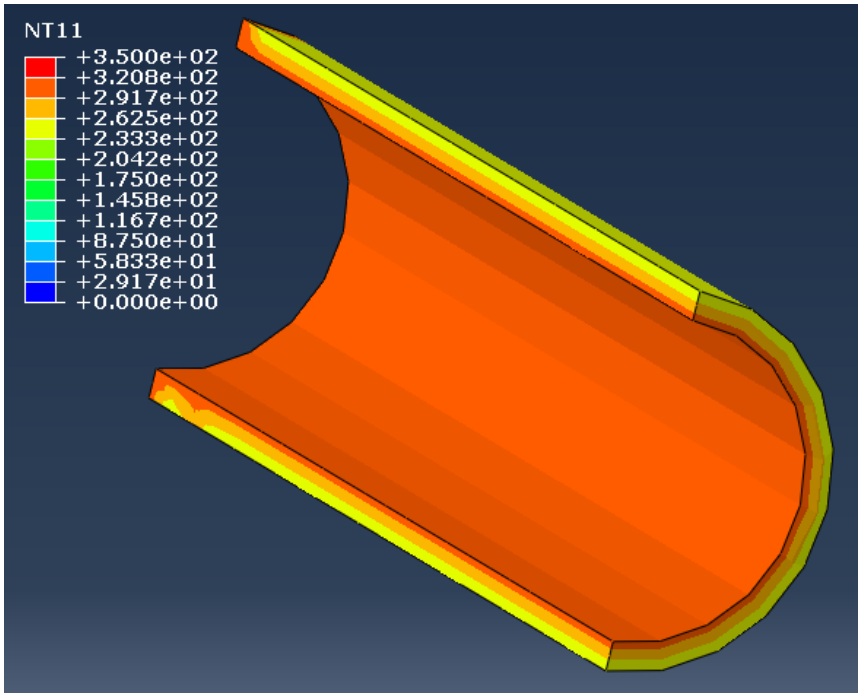

Figure 3.8 Closer view of spatial distribution of temperature in ID surface of HL at the end of 1900 sec

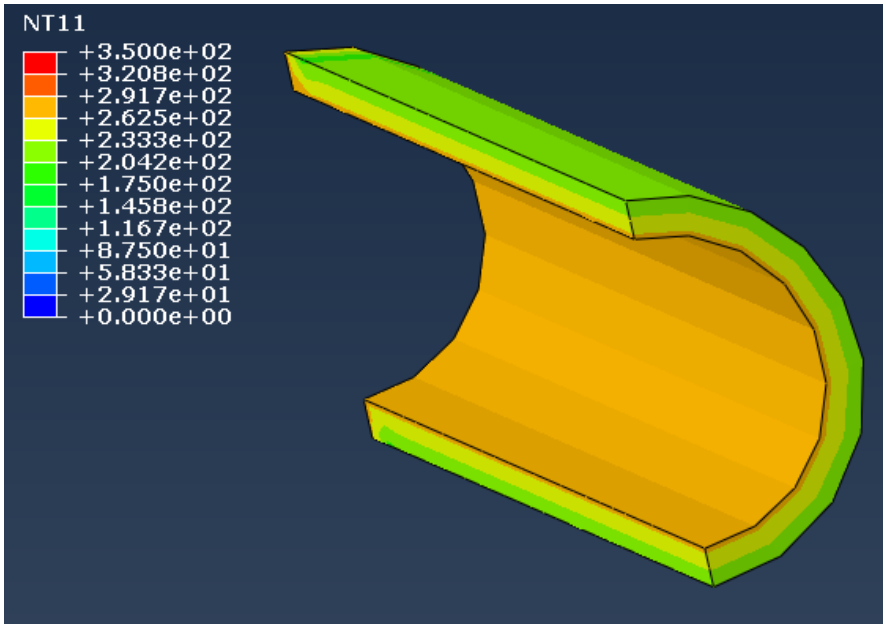

Figure 3.9 Closer view of spatial distribution of temperature in ID surface of CL at the end of 1900 sec

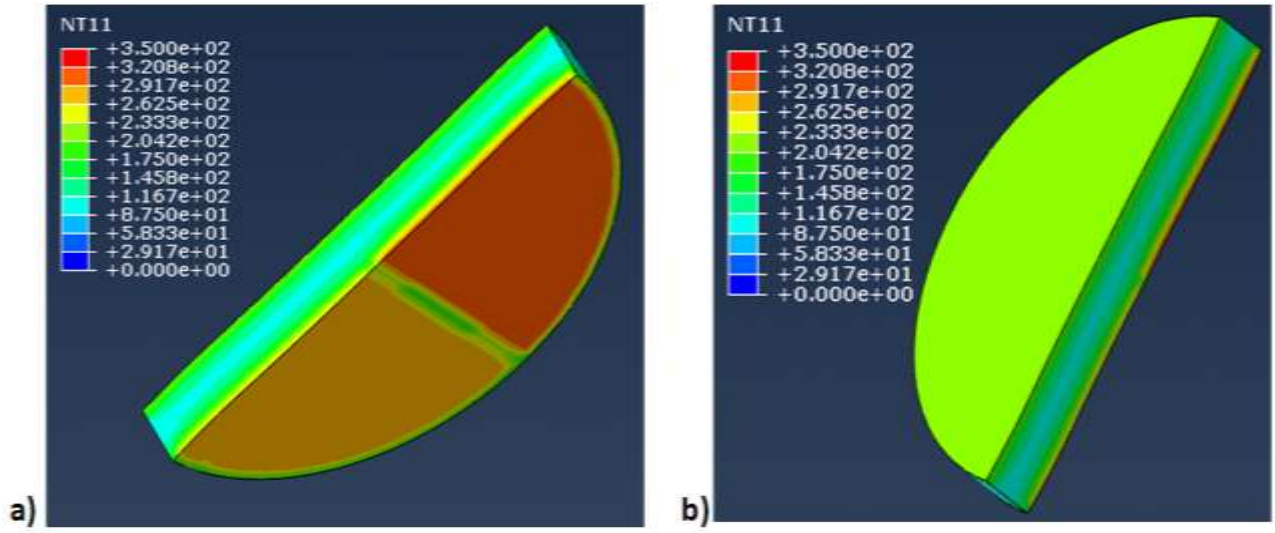

Figure 3.10 Closer view of spatial distribution of temperature in SG tube sheet at the end of 1900 sec at (a) bottom side (toward HL/CL) and (b) top side (toward feed water side)

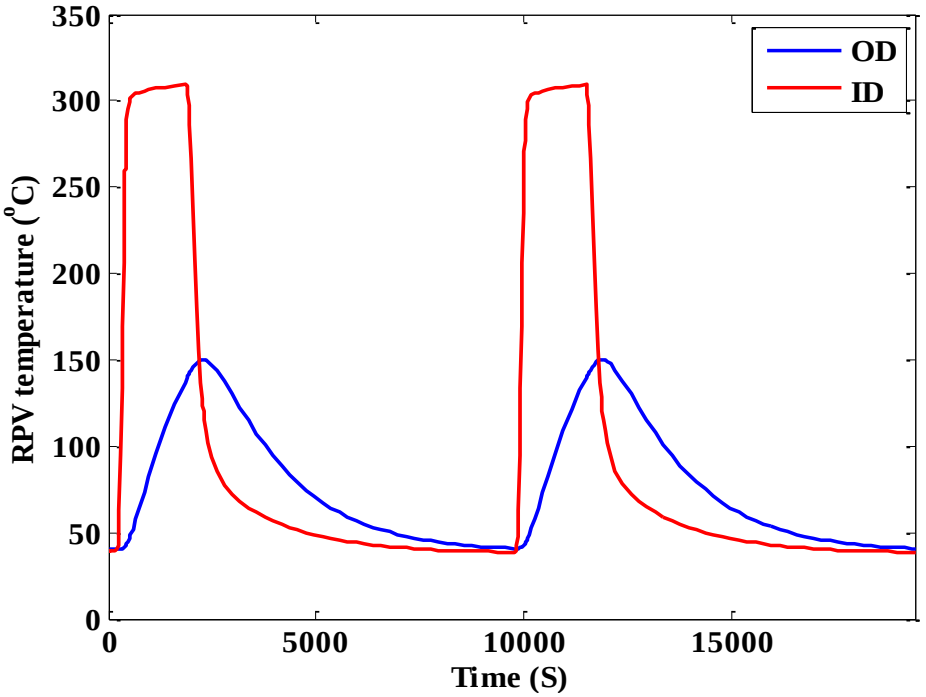

Figure 3.11 Time histories of simulated temperature at typical OD and ID nodes in mid-section of RPV

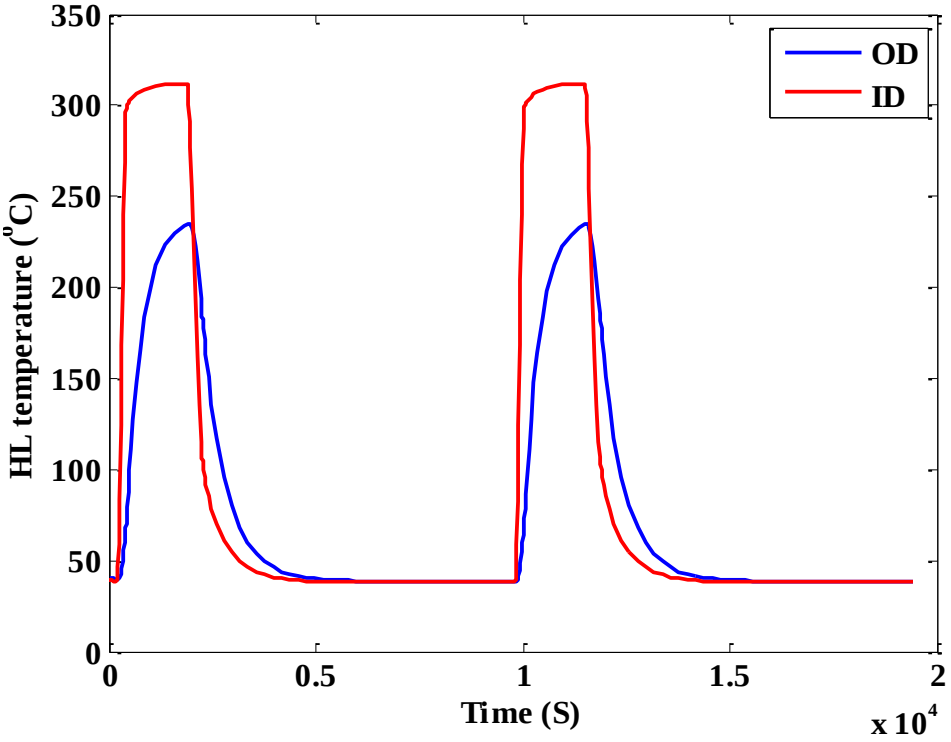

Figure 3.12 Time histories of simulated temperature at typical OD and ID nodes in elbow section of HL

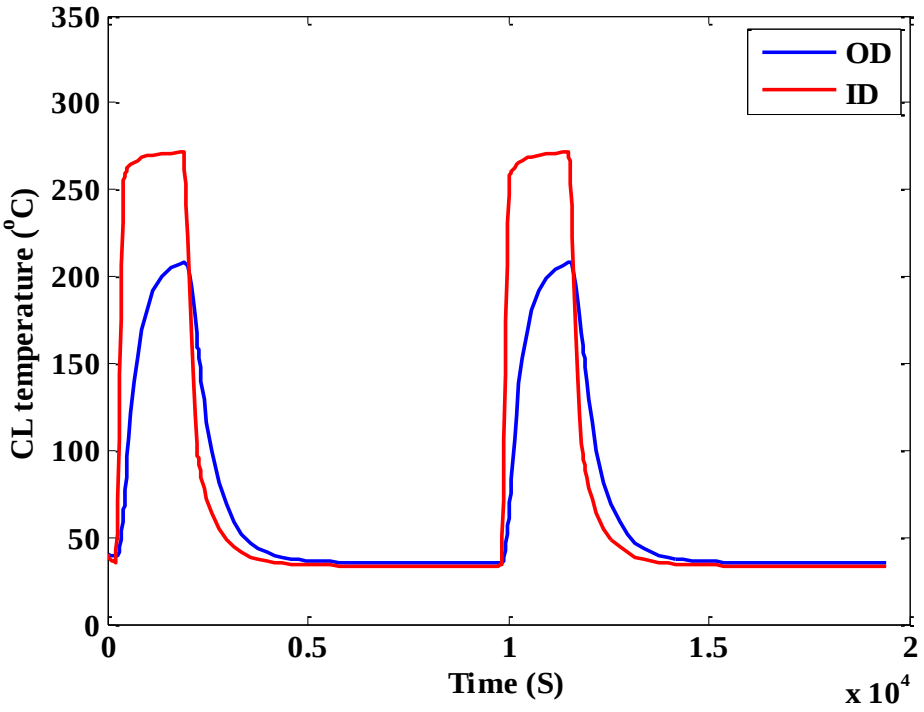

Figure 3.13 Time histories of simulated temperature at typical OD and ID nodes in elbow section of CL

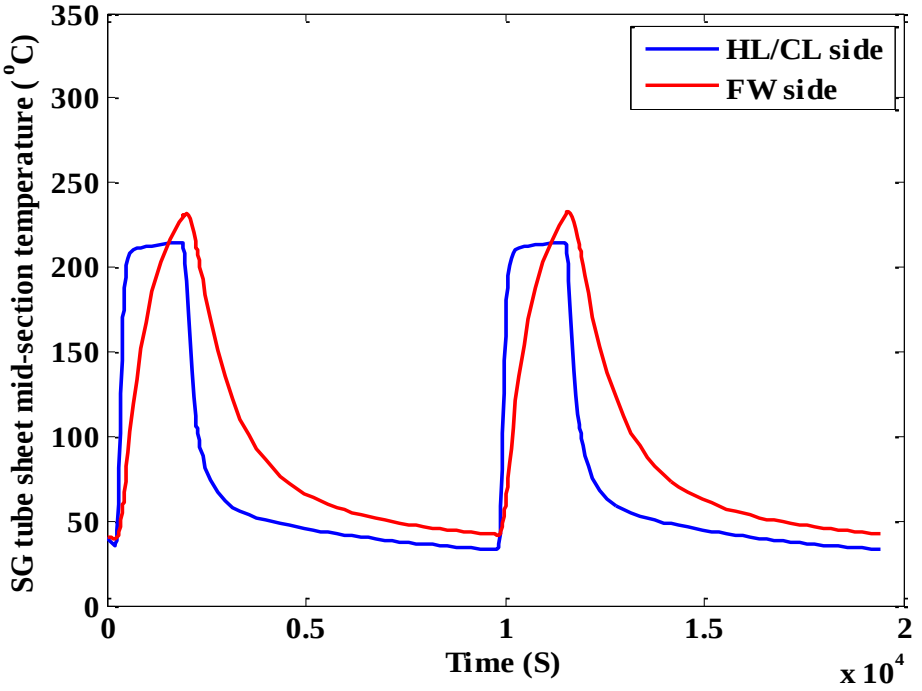

Figure 3.14 Time histories of simulated temperature at typical mid-section junction nodes in tube sheet of SG

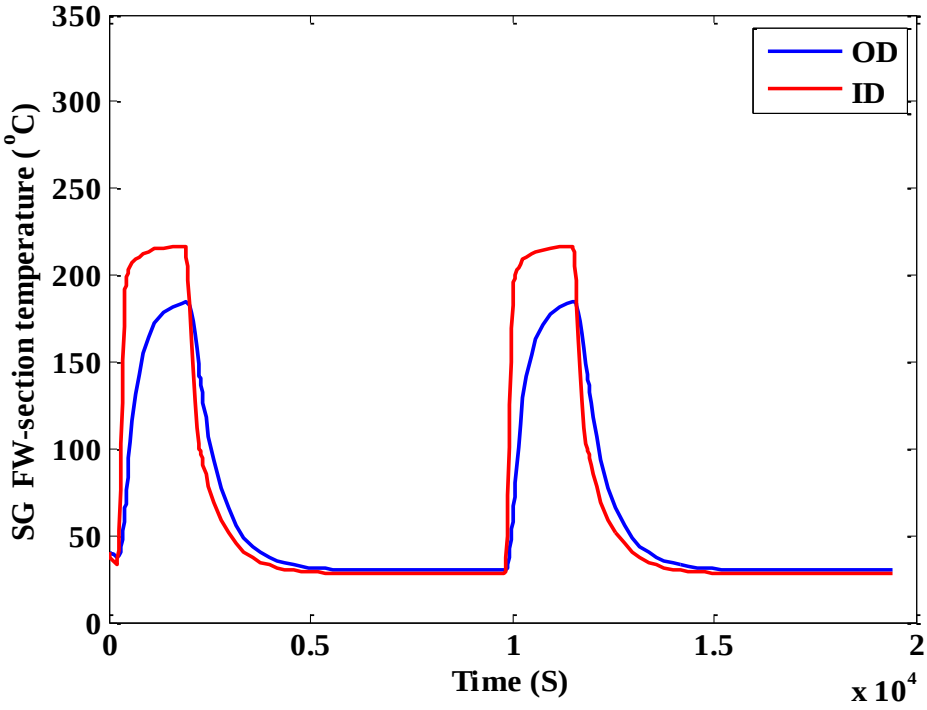

Figure 3.15 Time histories of simulated temperature at typical OD and ID nodes in feed water section of SG

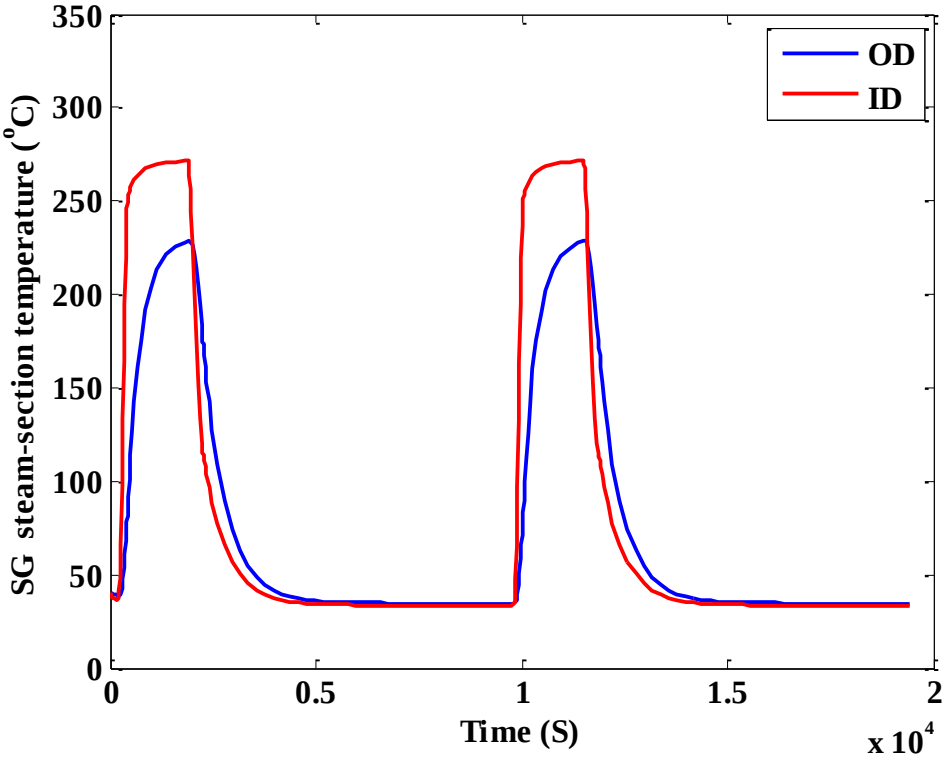

Figure 3.16 Time histories of simulated temperature at typical OD and ID FE nodes in steam section of SG

4 Results of Thermal-Mechanical Stress Analysis

We performed stress analyses using the system-level FE model for three cases: temperature loading, pressure loading, or both at the same time. For temperature loading, the nodal and time-dependent temperature distribution estimated through the heat transfer model was used in the structural analysis model to perform either pure thermal stress analysis (thermal load only) or sequentially coupled thermal-mechanical stress analysis. Separate stress analyses for temperature or pressure loading were performed to better understand the effect of individual loading components on overall stress analysis results performed under the combined thermal-mechanical load. The resulting stress analysis results were further considered for fatigue evaluation of some example components. The fatigue evaluation results will be discussed in the next section. Representative comparative stress analysis results are given below. Figures 4.1 and 4.2 show the von Mises and maximum principal stress distributions at the end of 1900 seconds (i.e., end of step 3 in Table 2.2), estimated for (a) pressure loading, (b) thermal loading, and (c) pressure and thermal loading. These figures show that the junction/nozzle area has higher von Mises and maximum principal stress compared to other regions. Because we did not take into account the nozzle material properties (e.g., dissimilar and similar metal thermal and mechanical properties), the actual absolute value of the stress at these hotspots may be quite different compared to our estimated values. We will include details of nozzle/weld material properties in a future FE model study. Also note that later in the present report, we discuss the fatigue life of some example components (e.g., HL and CL). Given that the present estimated nozzle stresses are not realistic, we thus did not consider the stress in the nozzle areas of the HL/CL in this fatigue evaluation. Instead, the stress and strain in the elbow region of the HL/CL were considered for the fatigue evaluation. Figure 4.3 shows the time histories for the maximum/minimum principal stress (σ_1/σ_3) at a typical ID element in the HL elbow for (a) pressure loading, (b) thermal loading, and (c) pressure and thermal loading. Similarly, Figure 4.4 shows the time histories of the maximum/minimum principal stress at a typical ID element in the CL elbow for the three loadings. For the HL case, the maximum principal stress (σ_1) for the combined pressure and thermal loading is much higher than those for the pressure or thermal only loadings. However, in the CL case, the maximum principal stress (σ_1) for the combined thermal and pressure loading is similar or slightly lower than that for thermal loading only. These different trends for the HL and CL cases could be due to multi-axial stress interaction. In addition, the maximum principal strains were estimated from different stress analysis models for comparative study and fatigue evaluation. For example, Figure 4.5 shows the maximum principal strain (ϵ_1) distributions at the end of 1900 seconds estimated for the three loadings. This figure indicates that the CL experiences higher strain compared to the HL. This effect is more evident for the pure thermal loading and combined pressure and thermal loading. The reason for higher stress in the CL could be due to the thinner section of the CL (thickness =55.88 mm) compared to the HL (thickness =60.96 mm). Due to the thinner section of CL, there is a steeper temperature gradient across the CL cross section compared to that across the HL cross section. This difference leads to both higher strain and stress in the CL compared to the HL. The higher principal stress in the CL compared to the HL is evident from Figures 4.3 and 4.4. Furthermore, the higher principal strain in the CL compared to the HL can also be seen by comparing Figures 4.6 and 4.7. Note that Figures 4.6 and 4.7 show the maximum/minimum strain (ϵ_1/ϵ_3) histories for stress analysis models with different loadings. From these figures, it also can be seen that, the maximum principal strain (ϵ_1) histories in the HL are largely compressive (particularly if thermal loading is applied), whereas in the case of the CL the maximum principal strain (ϵ_1) histories are tensile for all loading cases. In addition to the stress/strain comparisons, nodal displacements are presented. For example, Figure 4.8 shows the time histories for

nodal displacement (magnitude) at the end of 1900 sec for the three loadings. From this figure it can be seen that the SG nozzle ends of the HL and CL experience higher displacement for the thermal and pressure loading compared to the pressure or thermal loadings. Figures 4.9 and 4.10 show the time histories of nodal displacement magnitude (U_{mag}) at typical ID nodes in the end sections (near SG nozzle) of the HL and CL, respectively.

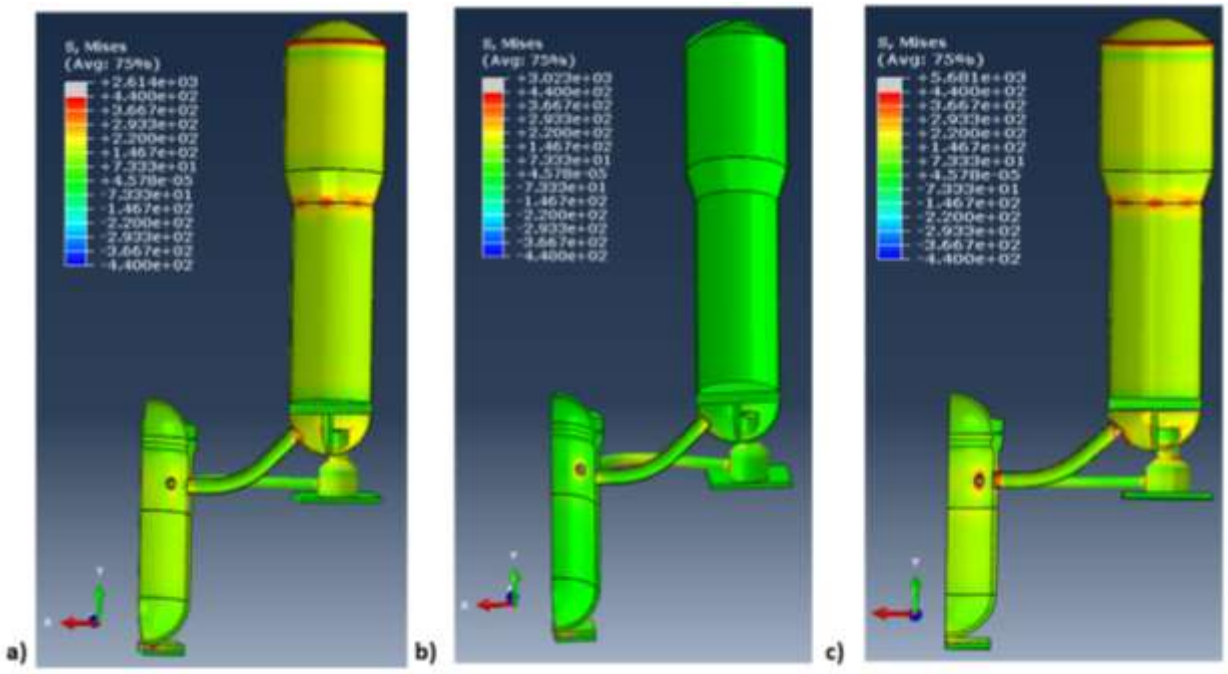

Figure 4.1 Von Mises stress distribution at the end of 1900 sec from stress analysis models with (a) pressure loading, (b) thermal loading, and (c) both pressure and thermal loading

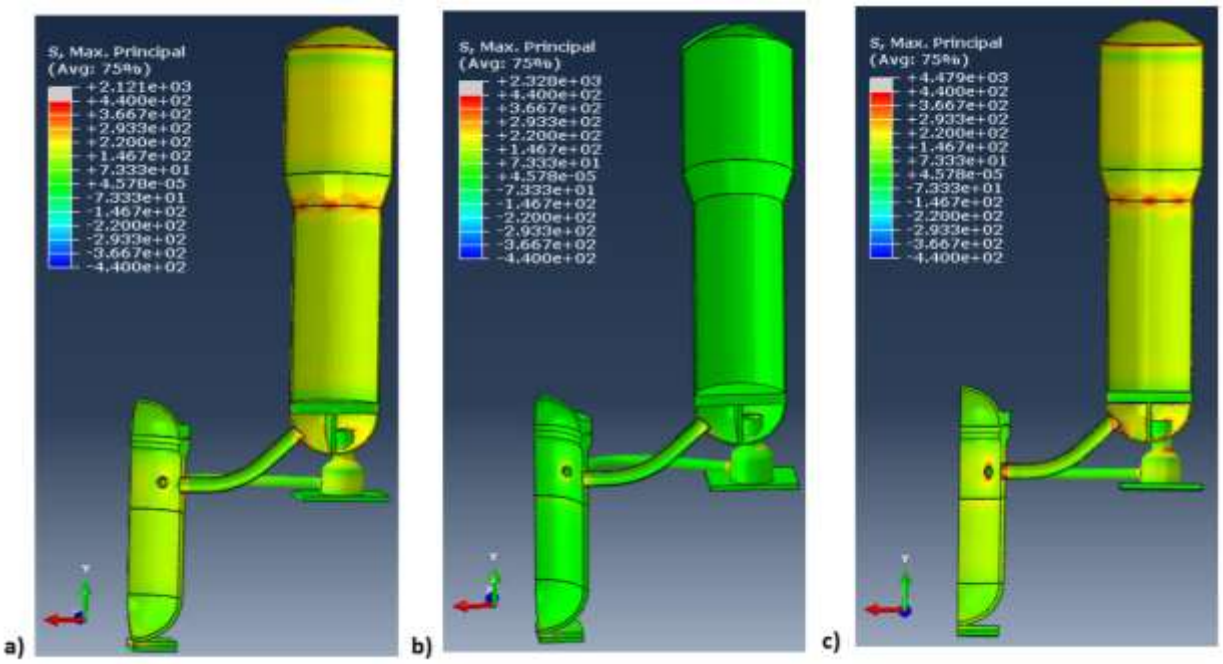

Figure 4.2 Maximum principal stress distribution at the end of 1900 sec from stress analysis models with (a) pressure loading, (b) thermal loading, and (c) both pressure and thermal loading

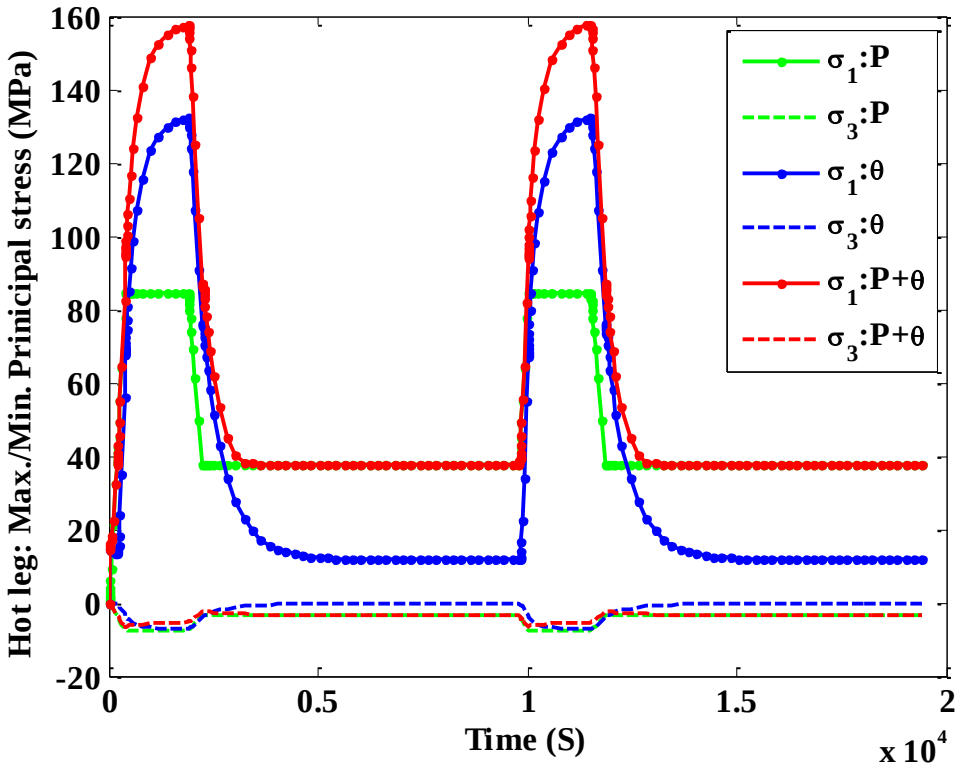

Figure 4 3 Maximum/minimum principal stress time histories at a typical ID element in the HL elbow from stress analysis models with pressure loading, thermal loading, and both pressure and thermal loading

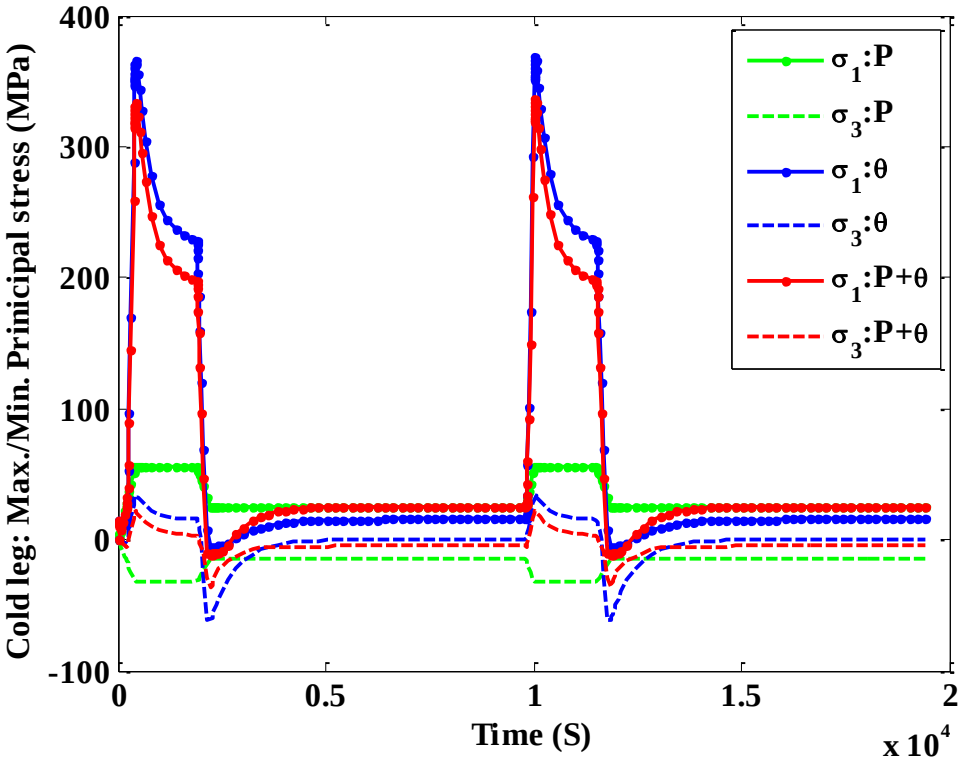

Figure 4.4 Maximum/minimum principal stress time histories at a typical ID element in CL elbow from stress analysis models with pressure loading, thermal loading, and both pressure and thermal loading

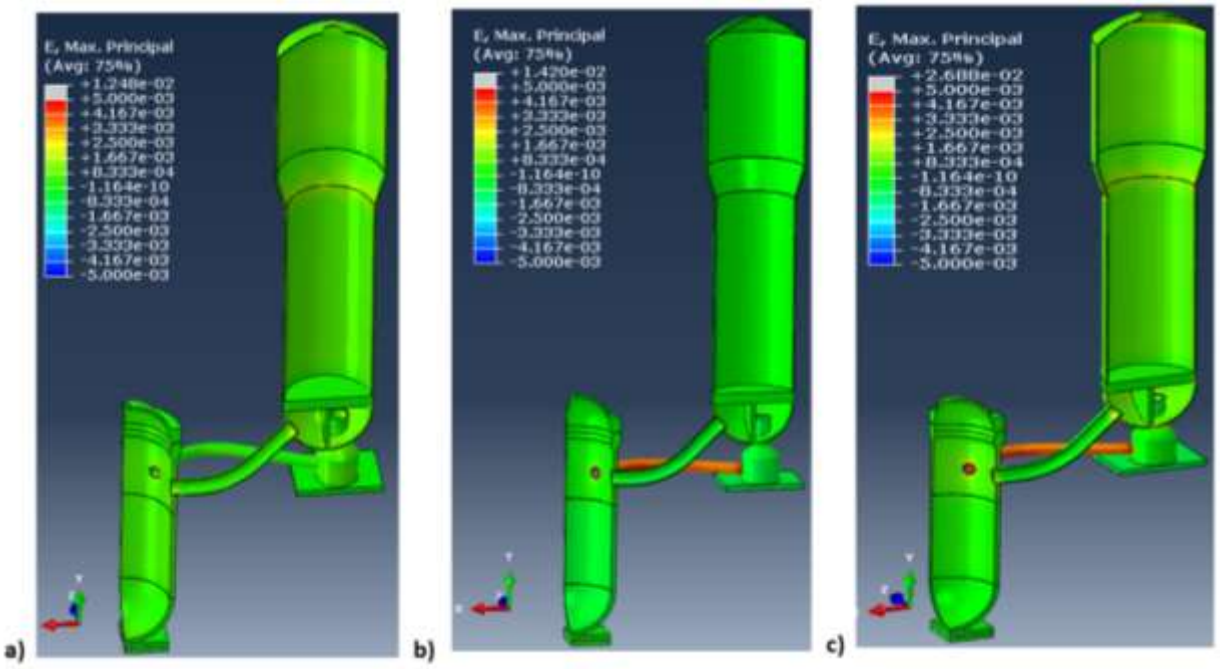

Figure 4.5 Maximum principal strain distribution at the end of 1900 sec from stress analysis models with (a) pressure loading, (b) thermal loading, and (c) both pressure and thermal loading

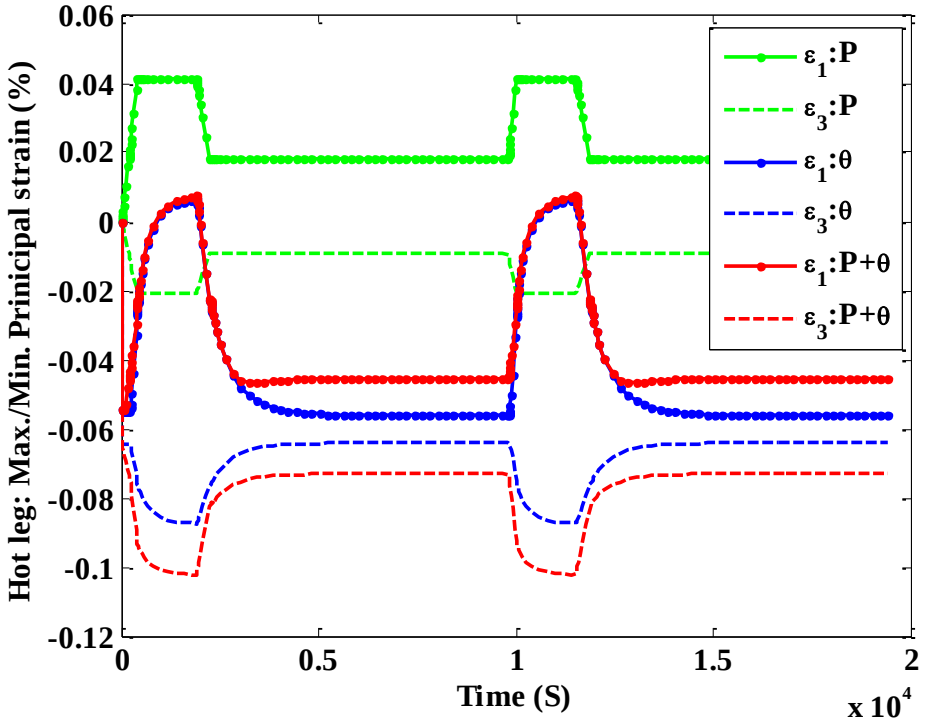

Figure 4.6 Maximum/minimum principal strain time histories at a typical ID element in HL elbow from stress analysis models with pressure loading, thermal loading, and both pressure and thermal loading

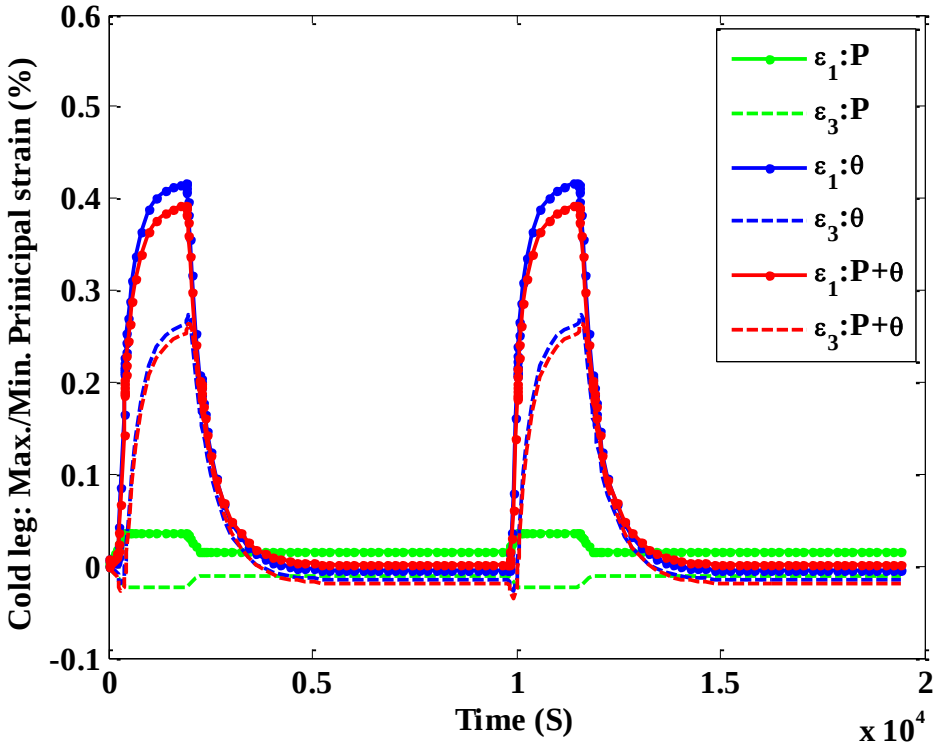

Figure 4.7 Maximum/minimum principal strain time histories at a typical ID element in CL elbow from stress analysis models with pressure loading, thermal loading, and both pressure and thermal loading

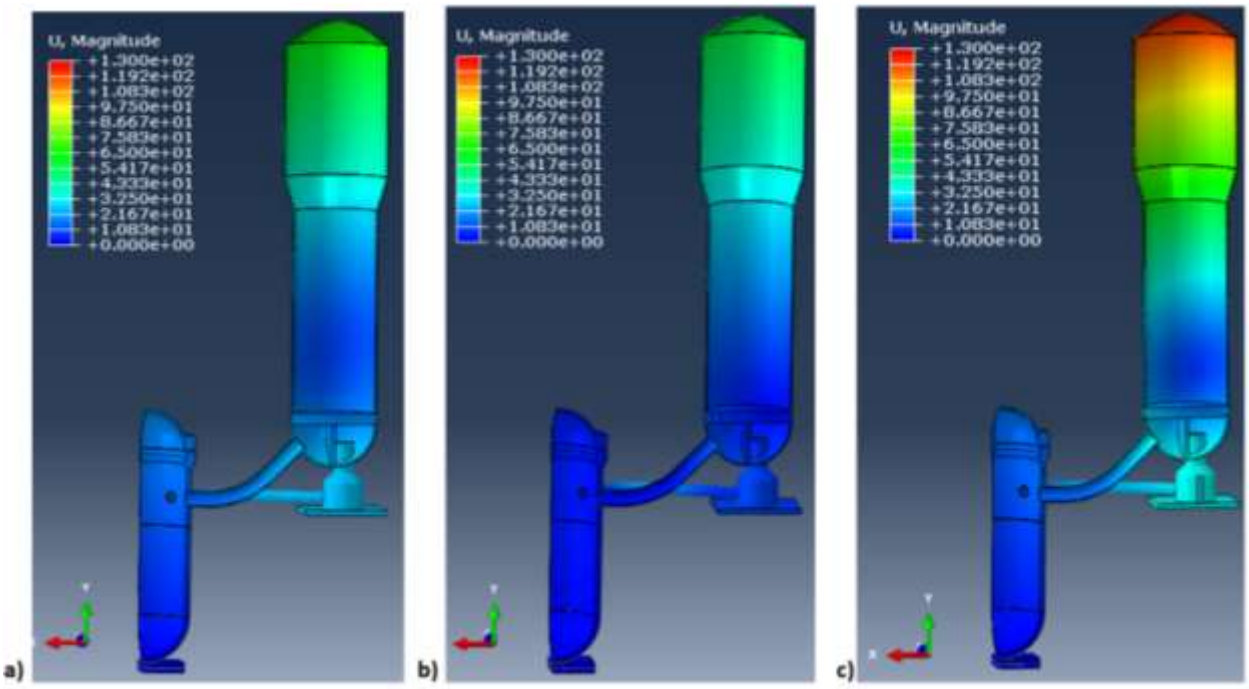

Figure 4.8 Displacement (magnitude) variation at the end of 1900 sec from stress analysis models with (a) pressure loading, (b) thermal loading, and (c) both pressure and thermal loading

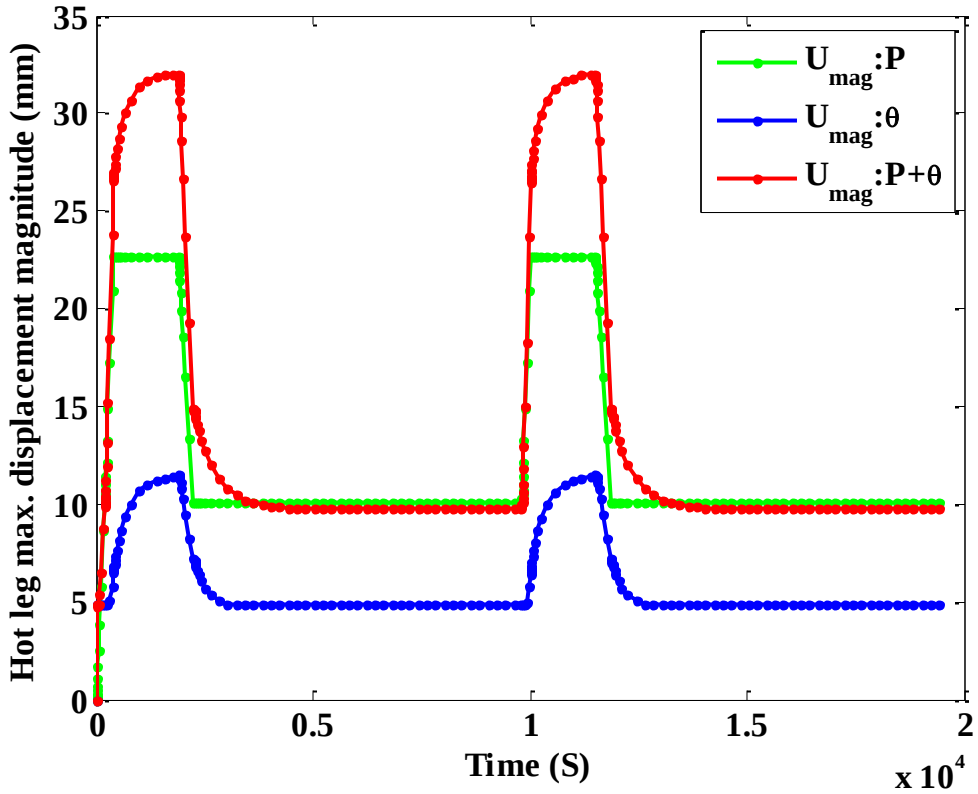

Figure 4.9 Maximum displacement time histories at a typical ID node in HL (near SG nozzle) from stress analysis models with pressure loading, thermal loading, and both pressure and thermal loading

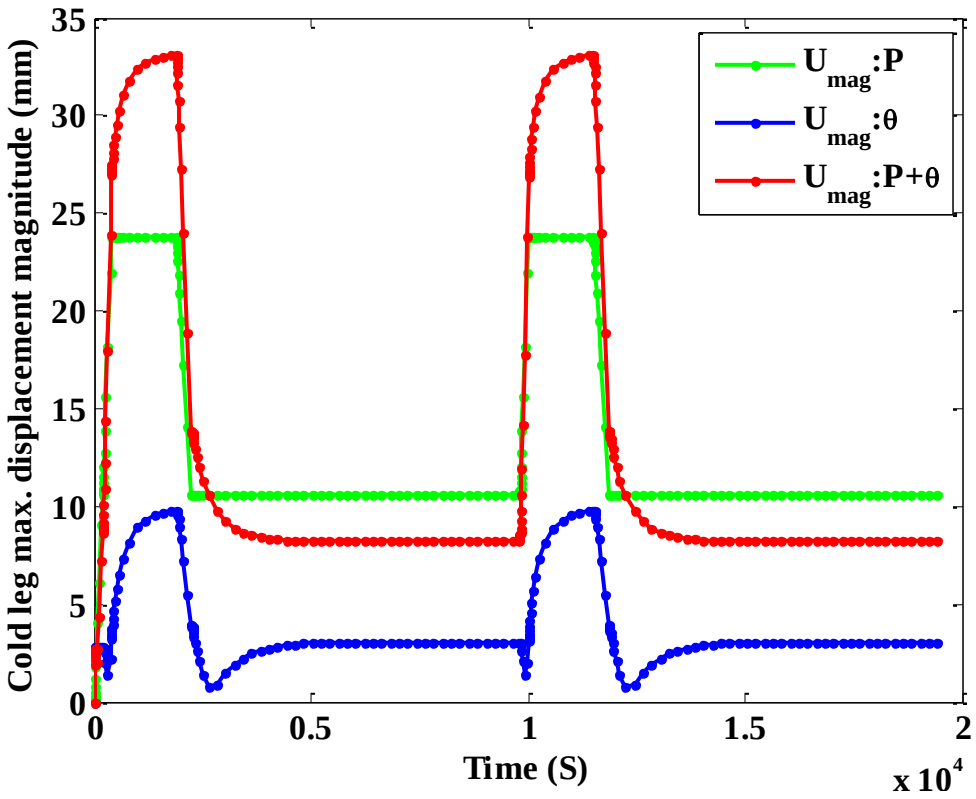

Figure 4.10 Maximum displacement time histories at a typical ID node in CL (near SG nozzle) from stress analysis models with pressure loading, thermal loading, and both pressure and thermal loading

5 Environmental Fatigue Life Estimation for Example Components

We performed preliminary fatigue analyses based on criteria from the ASME estimation of the in-air fatigue life [35] and from the NUREG-6909 estimation of the environmental fatigue life [21]. For the analyses, we chose two example components, such as the hot and cold legs. For the ASME-based fatigue evaluation, we used the maximum and minimum principal stress (σ_1 and σ_3) histories given in Figures 4.3 and 4.4 to estimate the equivalent cyclic stress amplitude σ_a using the following expression:

$$\sigma_a = \frac{1}{2}[max(\sigma_1(t) - \sigma_3(t)) - min(\sigma_1(t) - \sigma_3(t))] \quad (5.1)$$

Since, in the present example, both the thermal and pressure loadings yield the same stress/strain amplitude, only one fatigue cycle (say, cycle 2) was considered for the fatigue evaluation. Once the stress amplitude was estimated, we estimated the corresponding fatigue lives based on the in-air fatigue life curve for austenitic stainless steel given in the ASME code. For reference, the ASME in-air fatigue curve in SI units is given in Figure 5.1. While estimating the fatigue lives based on ASME fatigue curve, we made a necessary correction for the elevated temperature elastic modulus. The estimated in-air fatigue lives of the HL and CL under the three loading conditions are given in Tables 5.1 and 5.2, respectively.

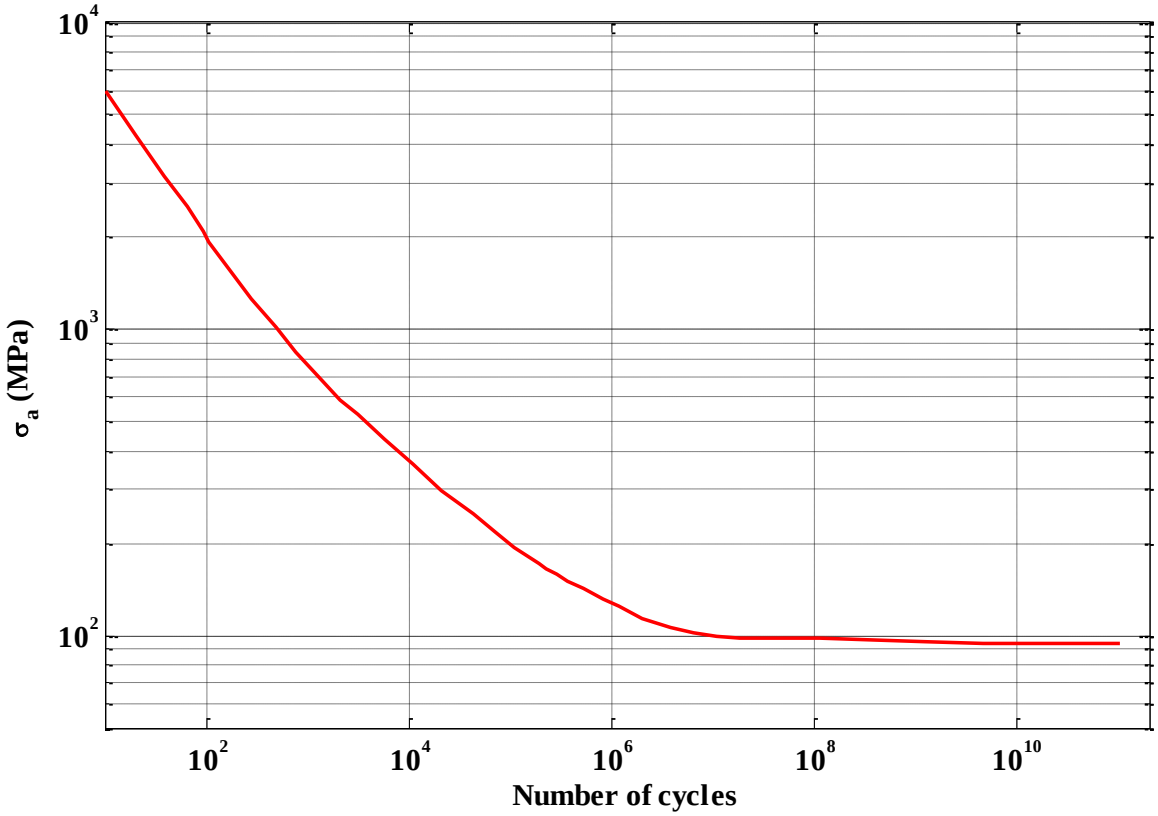

Figure 5.1 In-air fatigue design curve for austenitic stainless steel (ASME code [35])

Based on the estimated in-air condition fatigue lives (N_{air}), we then determined the lives under the PWR environment (N_{PWR}) based on the following equation for stainless steel under PWR conditions [21]:

$$N_{PWR} = \frac{N_{air}}{F_{en}} \tag{5.2}$$

where F_{en} is the environmental correction factor. For cast austenitic stainless steel, this factor is given as

$$F_{en} = \exp(-\theta' O' \dot{\epsilon}') \tag{5.3}$$

In Eq. 5.3, θ', O', and $\dot{\epsilon}'$ are transformed temperature, strain rate, and DO, respectively. For a maximum hot leg temperature of 315.56 ^{o}C and a maximum cold leg temperature of 275 ^{o}C, the transformed temperature θ' has the following form:

$$\theta' = \frac{(\theta - 100)}{250} \tag{5.4}$$

For strain rate $\dot{\epsilon} < 0.0004\ \%/s$, the transformed strain rate has the following form:

$$\dot{\epsilon}' = \ln(\frac{0.0004}{10}) \tag{5.5}$$

In Eq. 5.3, for PWR water O' is equal to 0.29. We determined the transformed strain rate $\dot{\epsilon}'$ in Eqs. 5.3 and 5.5 based on the estimated maximum strain rate. The maximum strain rate was estimated from the maximum cyclic strain amplitude. The expression for the maximum cyclic strain amplitude in terms of maximum and minimum principal strains (ϵ_1 and ϵ_3) is given below:

$$\epsilon_a = \frac{1}{2}[max(\epsilon_1(t) - \epsilon_3(t)) - min(\epsilon_1(t) - \epsilon_3(t))] \tag{5.6}$$

Using Eqs. 5.1 to 5.6 and the maximum and minimum principal strain histories in Figure 4.6 (for hot leg) and Figure 4.7 (for cold leg), the corresponding maximum strain amplitude (ϵ_a), strain rate ($\dot{\epsilon}$), and the environmental correction factor F_{en} were estimated under different loading conditions. Based on the estimated environmental correction factor, the previously estimated in-air fatigue lives were corrected by using Eq. 5.2. Note that NUREG-6909 suggests a threshold value of 0.1% strain amplitude, below which environmental effects on the in-air fatigue lives do not occur. Accordingly, if the strain amplitude is less than 0.1% (in this example, for the hot leg), the environmental correction factor is assumed to be equal to one, meaning there is no correction due to the environment. Tables 5.1 and 5.2 show the estimated maximum strain amplitude, strain rate, environmental correction factor, and associated fatigue lives under PWR conditions for the hot and cold legs, respectively.

Table 5.1 In-air and environmental fatigue lives estimated under different loading conditions for hot leg

Hot leg (based on elbow stress/strain)	Only pressure	Only temperature	Both temperature and pressure
Max. stress amplitude (MPa) (with elastic modulus correction)	28.811	71.928	69.049
Max. strain amplitude (%)	0.017297	0.042841	0.041126
Max. strain rate (%/s)	8.336e-06	2.0646e-05	1.982e-05
In-air fatigue life	$>10^6$	$>10^6$	$>10^6$
F_{en}	1	1	1
PWR environ. fatigue life	$>10^6$	$>10^6$	$>10^6$

Table 5.2 In-air and environmental fatigue lives estimated under different loading conditions for cold leg

Cold leg (based on elbow stress/strain)	Only pressure	Only temperature	Both temperature and pressure
Max. stress amplitude (MPa) (with elastic modulus correction)	27.685	180.87	171.18
Max. strain amplitude (%)	0.01662	0.11086	0.10481
Max. strain rate (%/s)	8.0102e-06	5.3429e-05	5.0512e-05
In-air fatigue life	$>10^6$	$1.1\text{x}10^5$	$1.9\text{x}10^5$
F_{en}	1	7.8124	7.8124
PWR environ. fatigue life	$>10^6$	14,080	24,320

6 Summary and Future Study

A system-level preliminary FE model was developed for a two-loop PWR reactor. This model was then used to conduct a system-level heat transfer analysis and subsequent thermal-mechanical stress analysis for typical design-basis thermal-mechanical cycles. The stress analysis results were then used to estimate in-air fatigue lives of components, such as the hot and cold legs, based on estimation criteria for the ASME in-air fatigue life and the fatigue design curve. Furthermore, estimated stress and strain histories were used to calculate environmental correction factors and associated PWR environment fatigue lives for the hot and cold legs based on the approach described in NUREG-6909. The discussed models and results are very preliminary. Further development of the model is required for more accurate life prediction of reactor components.

Suggested areas for the improvement of the discussed approach/models include the following:

1. Consideration of real plant transients for more realistic time-dependent heat transfer and structural analysis.
2. Inclusion of other components (surge line, pressurizer, etc.) and incorporation of more realistic geometric boundary conditions.
3. Detailed thermal-hydraulic simulation of key components for more realistic temperature boundary conditions (e.g., thermal stratification in surge line pipes during in-surge and out-surge).
4. Inclusion of elastic-plastic stress analysis for more accurate estimation of stress state beyond the elastic or yield limit.
5. Inclusion of evolutionary material models for inclusion of cyclic hardening and softening.
6. Use of weld material properties for accurate stress state estimation in the nozzle and other weld regions.
7. Weld modeling of the nozzle area and other weld regions for accurate inclusion of welding process-related residual stress.
8. Determination of the effect of preexisting notch/cracks and their propagation due to temperature and pressure cycling.
9. Consideration of other loading events such as pressurized thermal shock in addition to the heat-up/cool-down cycles.
10. Inclusion of radiation-induced swelling/shrinkage material models for more accurate stress state estimation of RPV.

References

1. Department of Energy, *The Nuclear Energy Advanced Modeling and Simulation (NEAMs) Program* (http://energy.gov/sites/prod/files/2013/07/f2/NEAMS%20Executive%20Program%20Plan.pdf).
2. Palmtag, S., Clarno, K., Davidson, G., Salko, R., Evans, T., Turner, J., & Schmidt, R. (2014). Coupled neutronics and thermal-hydraulic solution of a full core PWR using VERA-CS. Proceedings of International Topical Meeting on Advances in Reactor Physics (PHYSOR), Kyoto, Japan, September 28–October 3, 2014.
3. Kang, D. G., Jhung, M. J., & Chang, S. H. (2011). Fluid–structure interaction analysis for pressurizer surge line subjected to thermal stratification. *Nuclear Engineering and Design*, *241*(1), 257-269.
4. Conner, M. E., Hassan, Y. A., & Dominguez-Ontiveros, E. E. (2013). Hydraulic benchmark data for PWR mixing vane grid. *Nuclear Engineering and Design*, *264*, 97-102.
5. Yoon, H. Y., Cho, H. K., Lee, J. R., Park, I. K., & Jeong, J. J. (2012). Multi-scale thermal-hydraulic analysis of PWRs using the CUPID code. *Nuclear Engineering and Technology*, (8), 831-846.
6. Murase, M., Minami, N., Nagae, T., & Tomiyama, A. (2010). Countercurrent gas liquid flow in a PWR hot leg during reflux condensation. Dr. Valentin Uchanin (Ed.), InTech. Available from: http://www.intechopen.com/books/steam-generator-systems-operational-reliability-and-efficiency/countercurrent-flow-in-a-pwr-hot-leg-under-reflux-condensation.
7. Shan, J., Zhang, B., Gou, J., & Cao, L. (2014). *Subchannel Analysis, CFD Modeling and Verifications, CHF Experiments and Benchmarking*. Science and Technology of Nuclear Installations, Volume 2014, Hindawi Publishing Corporation.
8. Lin, T., Li, R., Long, H., & Ou, H. (2006). Three-dimensional transient sealing analysis of the bolted flange connections of reactor pressure vessel. *Nuclear Engineering and Design*, *236*(24), 2599-2607.
9. Yu, S., Liu, J., Zuo, W., & He, S. (2002). Sealing behavior of the HTR-10 pressure vessel flanges. *Nuclear Engineering and Design*, *216*(1), 247-253.
10. Jia, X., Chen, H., Li, X., Wang, Y., & Wang, L. (2014). A study on the sealing performance of metallic C-rings in reactor pressure vessel. *Nuclear Engineering and Design*, *278*, 64-70.
11. Mohanty, S., Majumdar, S., & Srinivasan, M. (2013). Constitutive modeling and finite element procedure development for stress analysis of prismatic high temperature gas cooled reactor graphite core components. *Nuclear Engineering and Design*, *260*, 145-154.
12. Mohanty, S., Jain, R., Majumdar, S., Tautges, T. J., & Makuteswara, S. Coupled thermal-irradiation-structural analysis of HGTR fuel brick using ABAQUS. Proceedings of ICAPP ’12, Chicago, June 24-28, 2012, Paper 12352.
13. Mohanty, S., Majumdar, S., & Natesan, K., Modeling of steam generator tube rupture using extended finite element method. Structural Mechanics in Reactor Technology (SMiRT)-22 Conference, San Francisco, California, August 18-23, 2013.
14. Chen, M., Lu, F., Wang, R., & Ren, A. (2014). Structural integrity assessment of the reactor pressure vessel under the pressurized thermal shock loading. *Nuclear Engineering and Design*, *272*, 84-91.
15. Qian, G., & Niffenegger, M. (2013). Procedures, methods and computer codes for the probabilistic assessment of reactor pressure vessels subjected to pressurized thermal shocks. *Nuclear Engineering and Design*, *258*, 35-50.

16. Qian, G., & Niffenegger, M. (2013). Integrity analysis of a reactor pressure vessel subjected to pressurized thermal shocks by considering constraint effect. *Engineering Fracture Mechanics*, *112*, 14-25.
17. Keim, E., Schmidt, C., Schöpper, A., & Hertlein, R. (2001). Life management of reactor pressure vessels under pressurized thermal shock loading: Deterministic procedure and application to Western and Eastern type of reactors. *International Journal of Pressure Vessels and Piping*, *78*(2), 85-98.
18. González-Albuixech, V. F., Qian, G., & Niffenegger, M. (2014). Integrity analysis of reactor pressure vessels subjected to pressurized thermal shocks by XFEM. *Nuclear Engineering and Design*, *275*, 336-343.
19. Qian, G., & Niffenegger, M. (2015). Investigation on constraint effect of a reactor pressure vessel subjected to pressurized thermal shocks. *Journal of Pressure Vessel Technology*, *137*(1), 011204.
20. Villanueva, W., Tran, C. T., & Kudinov, P. (2012). Coupled thermo-mechanical creep analysis for boiling water reactor pressure vessel lower head. *Nuclear Engineering and Design*, *249*, 146-153.
21. Chopra, O., and Stevens, G. (2014). *Effect of LWR Coolant Environments on the Fatigue Life of Reactor Materials*. U.S. Nuclear Regulatory Commission Report No. NUREG/CR-6909, Revision 1.
22. Japan Nuclear Energy Safety Organization (2011). *Nuclear Power Generation Facilities Environmental Fatigue Evaluation Method for Nuclear Power Plants*. Nuclear Energy System Safety Division, Japan Nuclear Energy Safety Organization Report No. JNES-SS-1005.
23. Gray, M. A., & Verlinich, M. M. (2012). *Guidelines for Addressing Environmental Effects in Fatigue Usage Calculations*. Electric Power Research Institute Report EPRI--1025823.
24. Chen, B. Y., Huang, C. C., Chou, H. W., Lin, H. C., Liu, R. F., Weng, T. L., & Chang, H. J. (2014). Reactor pressure vessel integrity assessment by probabilistic fracture mechanics–A plant specific analysis. *International Journal of Pressure Vessels and Piping*, *117*, 64-69.
25. Mohanty, S., Soppet, W. K., Majumdar, S. and Natesan, K. (2014). *Environmental Effect on Evolutionary Cyclic Plasticity Material Parameters of 316 Stainless Steel: An Experimental & Material Modeling Approach*. Argonne National Laboratory Report ANL/LWRS-14/1 (http://www.osti.gov/scitech/biblio/1168233).
26. Mohanty, S., Soppet, W. K., Majumdar, S.. and Natesan, K. (2013). *Report on Assessment of Environmentally-Assisted Fatigue for LWR Extended Service Conditions*. Argonne National Laboratory Report ANL/LWRS-13/3 (http://www.osti.gov/scitech/biblio/1168222).
27. Dassault Systèmes (2014). *ABAQUS Unified FEA: Complete Solutions for Realistic Simulation*. http://www.3ds.com/products-services/simulia/products/abaqus.
28. Shah, V. N., & MacDonald, P. E. (1993). *Aging and Life Extension of Major Light Water Reactor Components*. Elsevier Science.
29. Schulz, T. L. (2006). Westinghouse AP1000 advanced passive plant. *Nuclear Engineering and Design*, *236*(14), 1547-1557.
30. Cummins, W. E., Corletti, M. M., & Schulz, T. L. (2003). Westinghouse AP1000 advanced passive plant. In *Proceedings of ICAPP*, Vol. 3, pp. 4-7.
31. Westinghouse Electric (2000). *Westinghouse AP600 Design Control Document*. US-NRC Publication, ML003691016 (http://pbadupws.nrc.gov/docs/ML0036/ML003691016.html).
32. Westinghouse Electric (2011). *Westinghouse AP1000 Design Control Document*. US-NRC Publication, ML11171A500 (http://pbadupws.nrc.gov/docs/ML1117/ML11171A500.html).

33. International Atomic Energy Agency (2005). *Natural Circulation in Water Cooled Nuclear Power Plants Phenomena, Models and Methodology for System Reliability Assessments*. International Atomic Energy Agency Report ISEA-TECHDOC-1474.
34. Sengers, J. V., Watson, J. T. R., Basu, R. S., Kamgar-Parsi, B., & Hendricks, R. C. (1984). Representative equations for the thermal conductivity of water substance. *Journal of Physical and Chemical Reference Data*, *13*(3), 893-933.
35. American Society of Mechanical Engineers (2010). *ASME Boiler and Pressure Vessel Code*, section III.

This page intentionally left blank

Nuclear Engineering Division
Argonne National Laboratory
9700 South Cass Avenue, Bldg. 208
Argonne, IL 60439

www.anl.gov

Argonne National Laboratory is a U.S. Department of Energy
laboratory managed by UChicago Argonne, LLC